Experimental characterization of static and dynamic stall noise in an anechoic wind tunnel
ANR PIBE project - Final report Work Package 1

Benjamin Cotté, David Raus, Lisa Sicard, Romain Monchaux
ENSTA Paris, IMSIA, Palaiseau, France

Emmanuel Jondeau, Pascal Souchotte, Michel Roger
École Centrale de Lyon, LMFA, Ecully, France

June 13, 2024

Contents

1

Introduction

As explained by Oerlemans [1], local stall can occur on wind turbine blades during the upper part of the revolution in presence of a strong wind shear, or another source of inhomogeneous inflow such as yaw or topography. As a result, periodic separation and reattachment of the boundary layer can occur on the wind turbine blade suction side during its rotation. As stall noise is associated with a strong low-frequency increase [2, 3], this could explain the strong amplitude modulations of wind turbine noise that are commonly observed around wind farms.

The objective of Work Package 1 of the PIBE project (Predicting the Impact of Wind Turbine Noise) is to characterize static and dynamic stall noise in a controlled environment, in order to identify the flow structures that cause this phenomenon, and eventually to improve its modeling. For a static airfoil, a few studies have indeed been conducted to characterize separation/stall noise, see e.g. Refs. [2, 3, 4], and the mechanisms at the origin of the noise are more or less understood. For a pitching airfoil, on the other hand, the number of studies is limited [5, 6], and the turbulent structures at the origin of the noise are not clearly identified. In particular, the aerodynamic properties are known to vary significantly depending on the pitching frequency, with the presence of a dynamic stall vortex only above a given reduced frequency [7]. The work carried during this project is the first step towards the prediction of the amplitude modulations of wind turbine noise associated with dynamic stall noise.

This final report is organized as follows. First, the experimental setup is described in Section 2. Three different experimental campaigns have been conducted in the anechoic wind tunnel of the LMFA. The results of the first campaign with a NACA 0012 airfoil equipped with pressure taps are presented in Section 3. This airfoil has been used by other teams, and these measurements have enabled us to evaluate the performance of the setup Then, results from a second campaign with an instrumented NACA 63_3418 airfoil are detailed in Section 4. This airfoil section is classically used on wind turbine blades, and it appears that the airfoil shape plays an important role on the onset and development of dynamic stall. During the third campaign, described in Section 5, synchronous flow and acoustic measurements have been performed in order to identify the turbulent structures at the origin of static and dynamic stall noise.

Experimental setup

1 Wind tunnel and setup description

The experiments were performed in the anechoic wind tunnel of the Ecole Centrale de Lyon. This wind tunnel consists of an open jet with a rectangular $0.4 \, \text{m} \times 0.3 \, \text{m}$ nozzle exit, enclosed in an anechoic chamber of dimensions $8 \, \text{m} \times 9 \, \text{m} \times 10 \, \text{m}$, with a cut-off frequency below $100 \, \text{Hz}$. Two horizontal end-plates are installed downstream of the nozzle exit in order to guide the incoming flow. Two airfoils of chord $c = 12 \, \text{cm}$ and of span $s = 30 \, \text{cm}$ were tested: a NACA 0012 airfoil and a NACA 63_3418 airfoil, as detailed in Section 2. The airfoil leading edge is located $29 \, \text{cm}$ downstream of the nozzle outlet. Views of the experimental setups during the two campaigns are shown in Figure 2.1. During the second campaign, brushes are added at the curved edge of these end-plates to mitigate the scattering of the plate-boundary layer into acoustic waves. The airfoils were subjected to a flow of free-stream velocity U_∞, corresponding to a Reynolds number $Re_c = U_\infty c / \nu$ and a Mach number U_∞ / a, with ν the kinematic viscosity and a the sound speed. Measurements were conducted on vertical airfoils of chord $c = 0.12$ m and of span $s = 0.30$ m, the ends of which are clamped into discs that are integrated into the end-plates. The pitching motions of the airfoil are driven by a motor placed beneath the lower end-plate. The airfoil is centered on the discs so that it rotates about its center-chord.

In a given static configuration, measurements are performed at geometric angles of attack noted $\alpha_{s,g}$. In dynamic configurations, the sinusoidal motion was implemented as:

$$\alpha_{d,g} = \alpha_0 + \alpha_1 \sin\left(2\pi f_0 t\right), \tag{2.1}$$

where f_0 is the oscillation frequency, α_0 is the mean angle of attack and α_1 is the amplitude of the angle of attack variation. These angles are the geometric angles of attack fixed by the motor. The oscillation frequency f_0 is chosen so as the reduced frequency $k = \pi f_0 c / U_\infty$ is between 0.005 and 0.05. The precise values are given in the test matrices of Section 4. In an open-jet wind tunnel, the flow deviates from the nozzle axis because of the presence of the airfoil. The effective angles of attack of the airfoil are thus smaller than the geometric values. Incidence corrections can be applied, as shown in [8].

Three turbulence grids can be placed upstream in the wind tunnel to vary the turbulence intensity and integral length scale of the incident flow. The grid characteristics are

4

Figure 2.1: View of the experimental setups: (a) first campaign with NACA 0012 airfoil (b) second campaign with NACA 63$_3$418 airfoil.

	No grid	Grid 1	Grid 2	Grid 3
d_g (mm)	-	5.1	40	20
l_g (mm)	-	25	110	55
TI (%)	0.4	1.6	9	4.8
λ (mm)	-	8	20	14

Table 2.1: Characteristics of the turbulence grids used during the experimental campaigns. d_g et l_g correspond respectively to the bar width and to the opening width. TI and λ correspond respectively to the turbulence intensity and to the integral length scale of the flow downstream the grid.

given in Table 2.1. The measurements of the integral length scale λ and of the turbulence intensity $TI = u'_{rms}/U_\infty$, with u'_{rms} the root mean square value of the velocity fluctuations at the airfoil mid-span height are done using hot wire anemometry at 100 mm from the nozzle outlet.

2 Surface pressure and acoustic measurements

2.1 First campaign using a NACA 0012 airfoil

Measurements of the steady wall pressure on the airfoil are performed using 16 steady pressure taps at a sampling frequency $f_s = 100$ Hz, installed mid-span along the chord of the airfoil. See Figure 2.2(b). They are connected by a tubing system to a Kulite KMPS-1-64 pressure scanner. It is noteworthy that the steady pressure taps are mainly distributed on one side of the airfoil. In order to estimate the lift and moment coefficients of the airfoil by integrating the steady pressure along its two sides, it is therefore necessary to conduct experiments for both positive and negative angles of attack of the airfoil, so that the pressure taps are alternatively located on its suction and pressure sides. For

a given static configuration, measurements are thus performed for $\alpha_{s,g}$ and $-\alpha_{s,g}$, the sign of the angle of attack being defined in Figure 2.2(b). For dynamic configurations, measurements are performed for $\alpha_{d,g} = \alpha_0 + \alpha_1 \sin(2\pi f_0 t)$ and $\alpha_{d,g} = -\alpha_0 + \alpha_1 \sin(2\pi f_0 t)$, and post-synchronized during post-processing as explained hereafter.
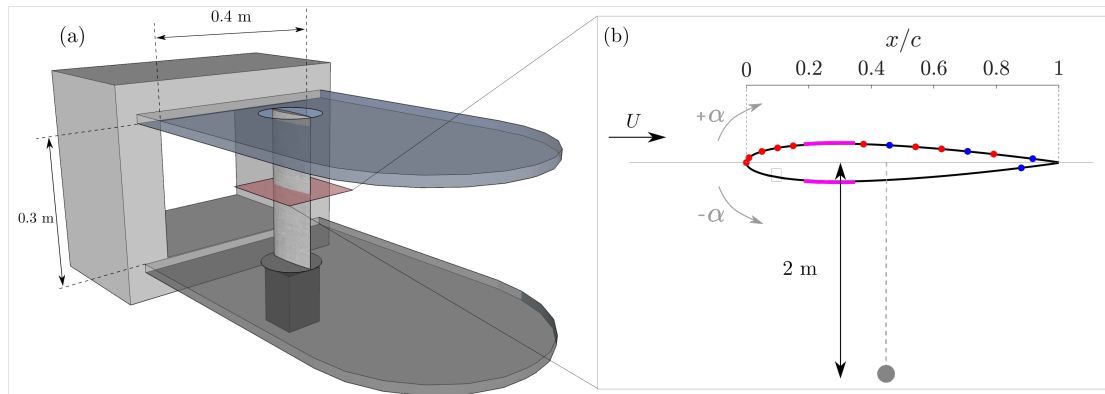

Figure 2.2: Schematic of the experimental setup: (a) Nozzle exit (b) Positions of the measuring points. Red dots and blue dots show the positions where only the steady-state surface pressure is measured and the positions where both the steady and fluctuating wall pressures are measured, respectively. The grey dot shows the position of the far-field microphone. Purple areas show the positions of the tripping tape. Figure 1b is not on scale.

The surface pressure fluctuations are measured by four Remote-Microphone Probes (RMP), located at four of the steady pressure tap positions (see blue dots in Figure 2.2(b)). The RMPs are equipped with Brüel & Kjær 4958 type microphones, and the signal acquisition is made at a sampling frequency $f_s = 51.2$kHz. The RMP dynamic response measurement and calibration method used here are described in Ref. [9].

The far-field noise is measured using 4 Gras 46BE microphones at a sampling frequency $f_s = 51.2$kHz, placed in the mid-span plane, 2 meters away from the airfoil center-chord and normal to the incoming flow direction. See Figure 2.3(a) and Table 2.3. It has been decided to place the microphones in the mid-span plane as the latter is known to be the location of major radiation for an airfoil at stall between two end-plates [10]. The acquisitions of the four remote microphone probes and of the far-field microphones are synchronized with the acquisition of the instantaneous angle of attack of the airfoil. The steady pressure taps measurements are synchronized with the microphones in the post-processing phase by comparing the signals of a steady pressure tap and of a remote microphone probe located at the same chord position. Background noise is measured by removing the airfoil and blowing at the same speed. It is assumed to be uncorrelated to the airfoil noise. However, for high incidences the background noise may be modified at low frequencies by the presence of the airfoil, due to interactions between the airfoil and the shear layers of the nozzle jet [2].

Measurements are performed for both clean and tripped airfoils, using 25 mm wide

tapes placed between $x/c = 0.16$ and $x/c = 0.36$ on both sides of the airfoil and along the entire span. Note that pressure taps 5 and 6 at $x/c = 21$ and 29% are hidden by the tripping tape.
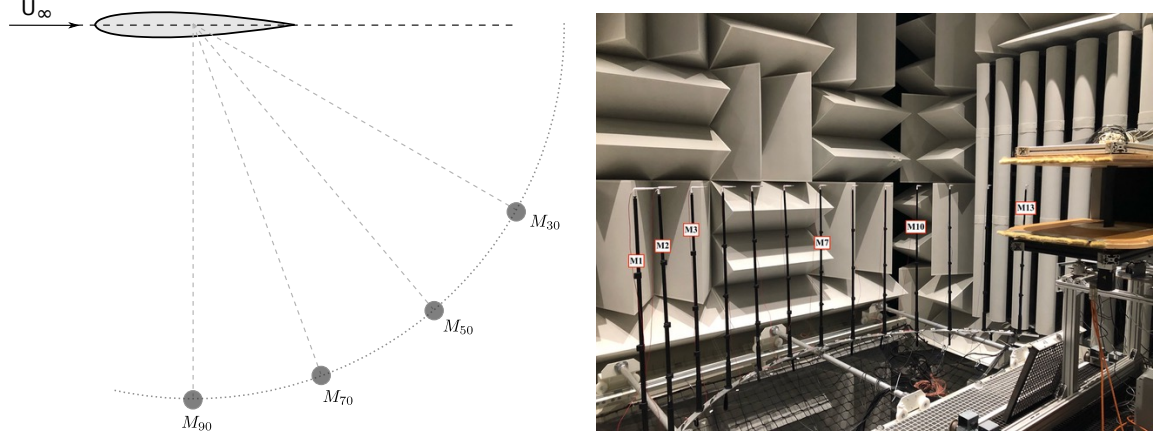
Figure 2.3: (a) Position of the 4 far-field microphones during the first campaign with a NACA 0012 airfoil (figure not to scale), and (b) view of the 13 far-field microphones during the second campaign with a NACA 63_3418 airfoil.

Number	LE	PS1	PS2	SS1	SS2	SS3	SS4	SS5	SS6
x (mm)	0	1	105	1	6	12	18	25	35
x/c (%)	0	1	88	1	5	10	15	21	29
RMP			🟩						

Number	SS6	SS7	SS8	SS9	SS10	SS11	SS12	SS13
x (mm)	35	45	55	65	75	85	95	110
x/c (%)	29	38	46	54	63	71	79	92
RMP			🟩			🟩		🟩

Table 2.2: Position of pressure taps for static pressure measurements. LE is on the leading edge, PS1 and PS2 are on the pressure side, and the other probes on the suction side. The pressure taps connected to remote microphone probes (RMP) are highlighted in green.

Number	1	2	3	4
θ (°)	30	50	70	90

Table 2.3: Angle θ of the far-field microphones with respect to the inflow velocity stream.

2.2 Second campaign using a NACA 63_3418 airfoil

The NACA 63_3418 airfoil is instrumented with 20 pinholes located mid-span, and 5 additional pinholes along the span at 10 mm from the trailing edge, as shown in Fig. 2.4 and in Tables 2.4, 2.5 and 2.6. The pin-holes located mid-span are connected by capillary tubes to a Kulite KMPS-1-64 pressure scanner to measure the wall pressure at a sampling frequency $f_s = 1.1$ kHz. Some of the pin-holes are also connected to Brüel & Kjær 4958 type microphones through a T-junction to acquire the fluctuating wall pressure signals at a sampling frequency $f_s = 51.2$ kHz. This Remote-Microphone Probe (RMP) technology and the in-situ calibration of the microphones is described in reference [11]. Note that the 5 pinholes located along the span are only connected to the remote microphone probes, as can be seen in Table 2.6.
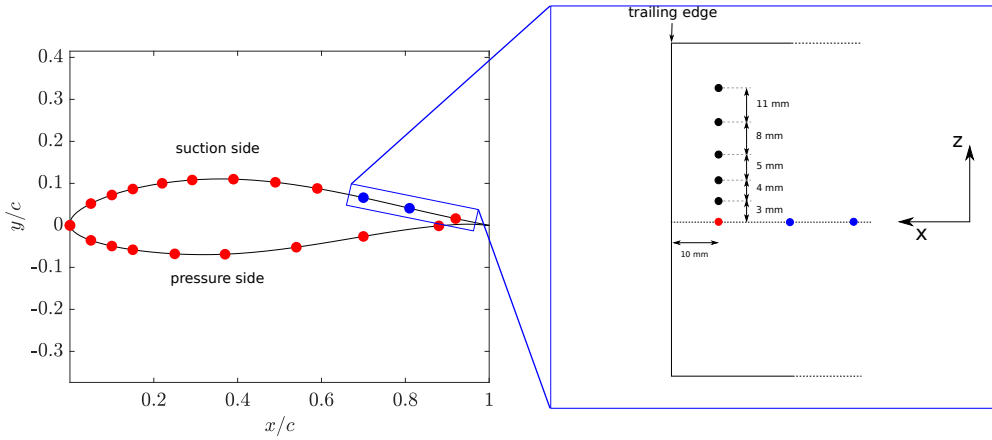

Figure 2.4: Positions of the pressure taps on the NACA 63_3418 airfoil in the mid-span plane (left) and along the span (right).

Far-field noise measurements were performed with a set of 13 Gras 46BE microphones placed in the mid-span, 2 meters away from the airfoil pressure side center-chord, as shown in Figure 2.3(b). The angles θ with respect to the direction of the inflow are given in Table 2.7, $\theta = 0$ corresponding to the downstream direction. In order to characterize the background noise generated by the wind tunnel and the end plates, far-field noise measurements are also performed in the same wind conditions but without the airfoil in the test section. The sources of the background noise (noise of the jet, trailing-edge noise of the horizontal plates...) are assumed to be identical when the airfoil is added in the test section. Precautions must be taken at very high angles of attack, as the background noise could be slightly modified at low frequencies because of the airfoil [2].

For the NACA63_3418, the tripping tape was only placed on the pressure side of the airfoil between $x/c = 0.1$ and $x/c = 0.15$. This tripping tape location was chosen because it prevents the generation of the laminar boundary layer tonal noise without heavily modifying the lift curve of the airfoil. Measurements are also performed without tripping tape and with turbulence grid 1, as the presence of inflow turbulence also suppresses laminar boundary layer tonal noise.

8

Number	1	2	3	4	5	6	7	8	9	10	11	12
Position x (mm)	0	6	12	18	26	35	47	59	71	84	97	110
Position (x/c)	0	0.05	0.1	0.15	0.22	0.29	0.39	0.49	0.59	0.7	0.81	0.92
Position z (mm)	0	0	0	0	0	0	0	0	0	0	0	0
Kulite static airfoil	🟩	🟩	🟩	🟩	🟩	🟩	🟩	🟩	🟩	🟩	🟩	🟩
RMP static airfoil		🟥		🟥	🟥	🟥	🟥	🟥	🟥	🟥	🟥	🟥
Kulite oscillating airfoil	🟩	🟩	🟩	🟩		🟩	🟩	🟩	🟩	🟩	🟩	🟩
RMP oscillating airfoil		🟥		🟥		🟥	🟥	🟥	🟥	🟥	🟥	🟥

Table 2.4: Position of pressure taps on the suction side of the airfoil. The pressure taps connected to the Kulite pressure scanner are highlighted in green, and the ones connected to remote microphone probes (RMP) are highlighted in red.

Number	13	14	15	16	17	18	19	20
Position x (mm)	6	12	18	30	44	65	84	106
Position (x/c)	0.05	0.1	0.15	0.25	0.37	0.54	0.7	0.88
Position z (mm)	0	0	0	0	0	0	0	0
Kulite Static airfoil	🟩	🟩	🟩	🟩	🟩	🟩	🟩	🟩
RMP Static airfoil					🟥		🟥	🟥
Kulite oscillating airfoil	🟩		🟩	🟩		🟩		🟩
RMP Dynamic oscillating airfoil					🟥		🟥	🟥

Table 2.5: Same as Table 2.4 for the pressure taps on the pressure side of the airfoil

Number	21	22	23	24	25
Position x (mm)	110	110	110	110	110
Position (x/c)	0.92	0.92	0.92	0.92	0.92
Position z (mm)	3	7	12	20	31
Kulite Static airfoil					
RMP Static airfoil	🟥	🟥	🟥	🟥	🟥
Kulite oscillating airfoil					
RMP oscillating airfoil	🟥	🟥	🟥	🟥	🟥

Table 2.6: Same as Table 2.4 for the pressure taps along the span of the airfoil at $x/c = 92\%$

3 Third campaign: Particle Image Velocimetry and acoustic measurements using a NACA 63_3418 airfoil

The measurements are performed for a NACA 63_3418 airfoil with the same dimensions as in Section 2, but without pressure taps. The velocity fields are measured using a two-dimensional Time-Resolved Particle Image Velocimetry (2D TR-PIV) system in the

Number	1	2	3	4	5	6	7	8	9	10	11	12	13
θ (°)	30	40	50	60	70	80	90	100	110	120	130	140	150
Oscillating airfoil													

Table 2.7: Angle θ of the far-field microphones with respect to the inflow velocity stream. The microphones used in the measurements on an oscillating airfoil are highlighted in blue.

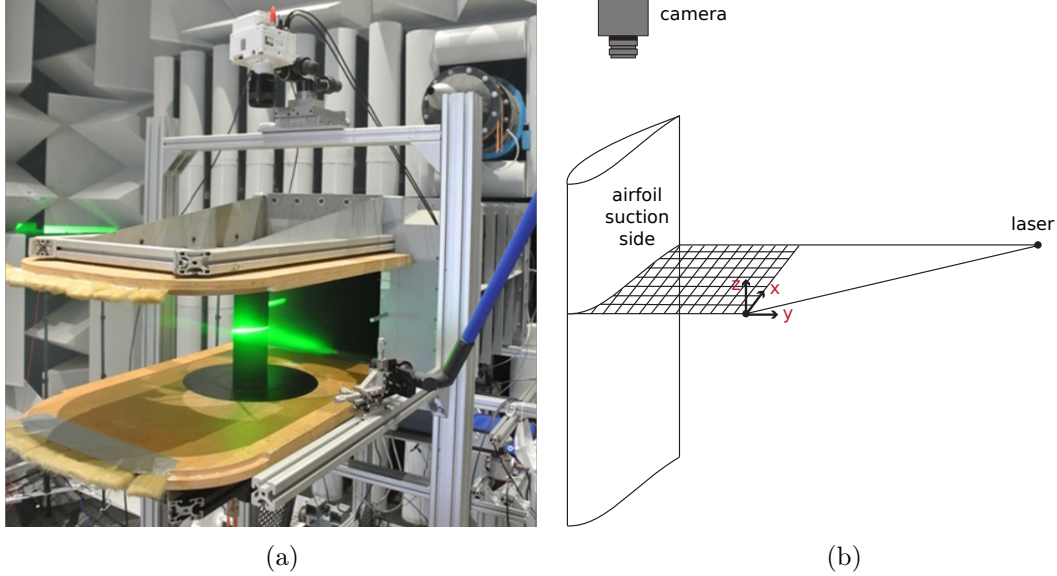(a)   (b)

Figure 2.5: (a) View of the experimental setup with 2D TR-PIV in the anechoic wind tunnel of LMFA, and (b) schematics of the measurement grid.

horizontal plane (x, y) on the airfoil suction side, as shown in Figure 2.5, with u' and v' the associated velocity fluctuations components. A Phantom VEO1310 camera is positioned above the upper guiding disc. To minimize the size of the area of the camera field located in the shadow of the airfoil, the camera is rotated around the z-axis by an angle of $-15°$ with the flow direction x. Moreover, to avoid light reflections generated by the airfoil wall, the camera is tilted around the x-axis by $+3°$ to the normal. The resulting distortion is corrected during the calibration step by using a three-dimensional calibration map. However, this tilt prevents the TR-PIV measurement to be valid close to the wall. Depending on the angle of attack and the position along the airfoil suction side, the thickness of this area without velocity field data varies between 10 mm at the leading edge and 1 mm at the trailing edge.

Velocity field measurements are performed ten times independently in a $166.8 \times 222 \, \text{mm}^2$ field of view with a spatial resolution of 5.76 px/mm. The TR-PIV sampling frequency is $f_{PIV} = 3 \, \text{kHz}$ with an acquisition duration of 1.65 s, thus 4953 images are recorded for each acquisition. The seeding is done with SAFEX Inside Nebelfluid

"Feuerwehr Extra" particles. They are injected at the compressor inlet, well upstream of the measurement zone. They then travel the entire length of the wind tunnel, ensuring a thorough homogenization of their distribution within the flow. Measurements of particle diameter using Phase Doppler Anemometry allowed us to obtain histograms revealing a size distribution ranging from $0.514\,\mu\text{m}$ to $3\,\mu\text{m}$, with an average particle diameter of around $1\,\mu\text{m}$. The particles are illuminated at 532 nm by a dual pulse laser, the Mesa PIV 532-120-M from Amplitude Laser$^{\circledR}$ delivering $9\,\text{mJ}$ per pulse, connected to an articulated arm. Data acquisition and processing are performed with the Lavision's Davis 10.1.2 software. A data preprocessing including a temporal filtering and a masking of the shadow zones is applied. Velocity vector fields are computed with a multi-pass cross-correlation algorithm with a final interrogation window size of 16×16 px^2 and an overlap of 50%. Selection criteria based on peak ratio and residual threshold values are applied in post-processing to eliminate spurious vectors.

Far-field acoustic measurements are performed using the same 13-microphone array as in the second campaign; see Table 2.7, with a sampling frequency $f_s = 51.2\,\text{kHz}$. The acquisition time is chosen equal to 2 seconds. It is longer than the TR-PIV acquisition time set to $1.65\,\text{s}$ to take into account the acoustic propagation time that is close to $6\,\text{ms}$. For each angle of attack in static conditions, the flow and acoustic measurements are carried ten times independently. For each oscillation frequency in dynamic conditions, several runs are also measured in order to have at least 20 complete cycles. In order to perform phase-averaging over a large number of cycles, additional acoustic measurements are also performed over 100 cycles without flow measurements. Finally, background noise measurements are performed over a period of $30\,\text{s}$ to characterize the noise generated by the wind tunnel, end plates and measuring devices.

4 Test matrices

4.1 First campaign using instrumented NACA 0012 airfoil

Static conditions

The information relative to the measurements for a static airfoil are given in Table 2.8. Measurements are performed for a duration of 30 s for angles of attack every 3 degrees from 0 to 30° at 25 and 50 m/s, and from 0 to 24° at 75 m/s.

Case	Date	U_∞ (m/s)	P_{atm} (Pa)	T_0 (°C)
No grid no trip	11/07/2019	25.8	98 352	23
		50.6	98 352	24
		76.1	98 352	25
No grid with trip	12/07/2019	25.7	98 387	28
		50.3	98 387	29
		75.2	98 387	30
With grid 1 no trip	12/07/2019	25.5	98 387	25
		49.8	98 387	25
		75.7	98 387	29
With grid 2 no trip	11/07/2019	24.5	98 352	25
		50.6	98 352	28
		75.0	98 352	25
With grid 3 no trip	11/07/2019	24.0	98 352	25
		49.4	98 352	25
		74.6	98 352	25

Table 2.8: Experimental conditions during the first campaign with a static NACA 0012 airfoil.

Dynamic conditions

The information relative to the measurements for an oscillating airfoil are given in Table 2.9. The parameters α_0, α_1, and f_0 associated with each experiment are detailed in Table 2.10. The durations are chosen so that 100 cycles are measured.

Case	Date	U_∞ (m/s)	P_{atm} (Pa)	T_0 (°C)
No grid no trip	17/07/2019	25.0	98 320	29
		50.3	98 320	28
		75.5	98 320	29
No grid with trip	17/07/2019	25.7	98 320	26
		49.4	98 320	29
With grid 3 no trip	18/07/2019	24.9	98 248	26
		50.0	98 248	29
		75.0	98 248	32

Table 2.9: Experimental conditions during the first campaign with an oscillating NACA 0012 airfoil.

Case	U_∞ (m/s)	(α_0, α_1) (°)	f_0 (Hz)	k	Duration (s)
No grid with trip	25	(5,7), (15,7), (15,15)	0.663	0.01	151
	25	(5,7), (15,7), (15,15)	1.326	0.02	76
	25	(5,7), (15,7), (15,15)	3.316	0.05	31
	50	(5,7), (15,7), (15,15)	1.326	0.01	76
	50	(5,7), (15,7), (15,15)	2.653	0.02	38
No grid no trip	25	(5,7), (15,7), (15,15)	0.332	0.005	302
	25	(5,7), (15,7), (15,15)	0.663	0.01	151
	25	(5,7), (15,7), (15,15)	1.326	0.02	76
	25	(5,7), (15,7), (15,15)	3.316	0.05	31
	50	(5,7), (15,7), (15,15)	0.663	0.005	151
	50	(5,7), (15,7), (15,15)	1.326	0.01	76
	50	(5,7), (15,7), (15,15)	2.653	0.02	38
	75	(5,7), (15,7), (15,15)	0.995	0.005	101
	75	(5,7), (15,7), (15,15)	1.989	0.01	51
	75	(5,7), (15,7), (15,15)	3.979	0.02	26
With grid 3 no trip	25	(5,7), (15,7), (15,15)	0.332	0.005	302
	25	(5,7), (15,7), (15,15)	0.663	0.01	151
	25	(5,7), (15,7), (15,15)	1.326	0.02	76
	25	(5,7), (15,7), (15,15)	3.316	0.05	31
	50	(5,7), (15,7), (15,15)	0.663	0.005	151
	50	(5,7), (15,7), (15,15)	1.326	0.01	76
	50	(5,7), (15,7), (15,15)	2.653	0.02	38
	75	(5,7), (15,7), (15,15)	0.995	0.005	101
	75	(5,7), (15,7), (15,15)	1.989	0.01	51
	75	(5,7), (15,7), (15,15)	3.979	0.02	26

Table 2.10: Parameters associated with the first campaign with an oscillating NACA 0012 airfoil.

4.2 Second campaign using instrumented NACA 63_3418 airfoil

Static conditions

During the second campaign, the measurements of the static pressure with the Kulite pressure scanner and of the dynamic and acoustic pressure with RMP and far-field microphones have been performed during different days. Table 2.11 and Table 2.12 detail the experimental conditions during the static pressure measurements and dynamic or acoustic pressure measurements respectively. Measurements are performed during a duration of 20 seconds for the static pressure, and of 30 seconds for the dynamic and acoustic pressure. Angles of attack are varied every degree between -5 and 30° (or between 0 and 30° in some cases).

Case	Date	P_{atm} (Pa)	T_0 (°C)
No grid no trip	05/11/2020	100 012	15
No grid with trip	01/12/2020	98 698	8
With grid no trip	17/11/2020	99 571	16

Table 2.11: Experimental conditions during the second campaign with a static NACA 63_3418 airfoil for the measurement of static pressure.

Case	Date	P_{atm} (Pa)	T_0 (°C)
No grid no trip	30/11/2020	99 329	8
No grid with trip	04/12/2020	95 677	10
With grid no trip	17/11/2020	98 878	9

Table 2.12: Experimental conditions during the second campaign with a static NACA 63_3418 airfoil for the measurement of RMP and far-field acoustic pressure.

Dynamic conditions

The information relative to the experimental conditions for an oscillating NACA 63_3418 airfoil can be found in Table 2.13. The parameters α_0, α_1, and f_0 associated with each experiment are detailed in Table 2.14. The durations are chosen so that 100 cycles are measured. Note that the measurement for $f_0 = 6.631\,\mathrm{Hz}$ and $U_\infty = 50\,\mathrm{m/s}$ is only performed in the case without grid and with trip. The motor has difficulties reaching such a high value of the oscillation frequency.

Case	Date	P_{atm} (Pa)	T_0 (°C)
No grid with trip	14/12/2020	98 076	10
With grid no trip	14/12/2020	98 076	10

Table 2.13: Experimental conditions during the second campaign with an oscillating NACA 63_3418 airfoil

U_∞ (m/s)	α_0 (°)	α_1 (°)	f_0 (Hz)	k	Duration (s)
25	15	5, 10 or 15	0.663	0.01	151
25	15	5, 10 or 15	1.658	0.025	61
25	15	5, 10 or 15	3.316	0.05	31
25	15	5, 10 or 15	4.974	0.075	21
50	15	5, 10 or 15	0.663	0.005	151
50	15	5, 10 or 15	1.326	0.01	76
50	15	5, 10 or 15	3.316	0.025	31
50^1	15	5, 10 or 15	6.631	0.05	16
75	15	5, 10 or 15	0.995	0.005	101
75	15	5, 10 or 15	1.989	0.01	51
75	15	5, 10 or 15	4.974	0.025	21

Table 2.14: Parameters associated with the dynamic conditions in the configurations no grid with trip and with grid no trip.

4.3   Third campaign with TR-PIV using NACA 63_3418 airfoil

Static conditions

Far-field acoustic measurements have first been performed using the 13-microphone array during 30 seconds, as given in Table 2.15. Then, synchronized TR-PIV and acoustic measurements have been recorded for six angles of attack: 0°, 2°, 15°, 18°, 27°, 30° . The experimental conditions related to these synchronized measurements are given in Table 2.16.

Case	Date	P_{atm} (Pa)	T_0 (°C)
No grid with trip	27/01/2021	98 613	8
With grid no trip	27/01/2021	98 613	8

Table 2.15: Experimental conditions during the third campaign with a static NACA 63_3418 airfoil for the measurement of far-field acoustic pressure only.

Case	U_∞ (m/s)	N_{runs}	Date	α_g (°)
No grid with trip	$U_\infty = 25\,\mathrm{m/s}$	20	23/02/2021	0, 2, 15, 27
			24/02/2021	30
			25/02/2021	18
No grid with trip	$U_\infty = 50\,\mathrm{m/s}$	10	26/02/2021	all
With grid no trip	$U_\infty = 50\,\mathrm{m/s}$	5	09/03/2021	all
No grid no trip	$U_\infty = 50\,\mathrm{m/s}$	5	09/03/2021	27

Table 2.16: Experimental conditions during the third campaign with a static NACA 63_3418 airfoil for the TR-PIV and acoustic measurements.

Dynamic conditions

Far-field acoustic measurements have first been performed using the 13-microphone array for a duration of 100 cycles, as given in Table 2.17. Then, synchronized TR-PIV and acoustic measurements have been recorded in the experimental conditions detailed in Table 2.18.

Case	Date	P_{atm} (Pa)	T_0 (°C)
No grid with trip	12/01/2021	99 119	4
With grid no trip	13/01/2021	99 096	9

Table 2.17: Experimental conditions during the third campaign with an oscillating NACA 63_3418 airfoil for the measurement of far-field acoustic pressure only.

Case	U_∞ (m/s)	f_0 (Hz)	k	N_{runs}	Date
No grid with trip	25	0.660	0.01	21	25/02/2021
	25	1.660	0.025	15	25/02/2021
	25	3.320	0.05	8	25/02/2021
	25	4.974	0.075	5	25/02/2021
No grid with trip	50	0.660	0.005	20	26/02/2021
	50	1.326	0.01	10	26/02/2021
	50	3.316	0.025	5	26/02/2021
	50	4.974	0.0375	5	08/03/2021
	50	6.600	0.05	2	08/03/2021
With grid no trip	50	0.660	0.01	20	09/03/2021
	50	1.326	0.02	10	09/03/2021
	50	3.316	0.05	5	09/03/2021
	50	6.600	0.1	2	09/03/2021
No grid no trip	50	3.316	0.025	5	09/03/2021

Table 2.18: Experimental conditions during the third campaign with an oscillating NACA 63_3418 airfoil for the TR-PIV and acoustic measurements ($\alpha_0 = \alpha_1 = 15°$).

Results of the first campaign using an instrumented NACA 0012 airfoil

In this chapter, results from the first campaign using a NACA 0012 airfoil are presented . First, the influence of turbulence intensity and surface tripping are examined in Section 1. Then, a detailed analysis of stall noise in static conditions is presented in Section 2 in the case without turbulence grid and with tripping. Finally, the effect of the airfoil oscillation on the stall noise characerics are investigated in Section 3. Some of the results presented in this chapter are extracted from the article of Raus *et al.* [8] published in the Journal of Sound in Vibration in 2022.

1 Influence of turbulence intensity and of surface tripping on the aerodynamics and on the noise radiation

1.1 Effect of the turbulence intensity on the aerodynamics

Before examining the far-field noise radiated by the airfoil, we study first the influence of the inflow turbulence intensity TI on the aerodynamic coefficients. The lift coefficient C_l and moment coefficient at the quarter chord $C_{m\frac{1}{4}}$ are obtained by integrating the static pressure around the airfoil for each angle of attack. The evolution of C_l and $C_{m\frac{1}{4}}$ with respect to the geometric angle of attack is plotted in Figure 3.1. Although the angle of attack resolution is quite poor (3°), it appears that there is a critical angle above which the lift coefficient drops and the moment coefficient changes sign. Two effects of the turbulence intensity are visible in Figure 3.1. Firstly, the increase of TI causes a stall delay, associated with an increase in the lift maximum value before stall. Secondly, the sudden drop of lift observed for low turbulence intensities become less intense when TI increases. These two results are in agreement with Devinant *et al.* [12], who also show that an increase of the inflow turbulence delays the motion of the separation point towards the leading edge for trailing edge stall.
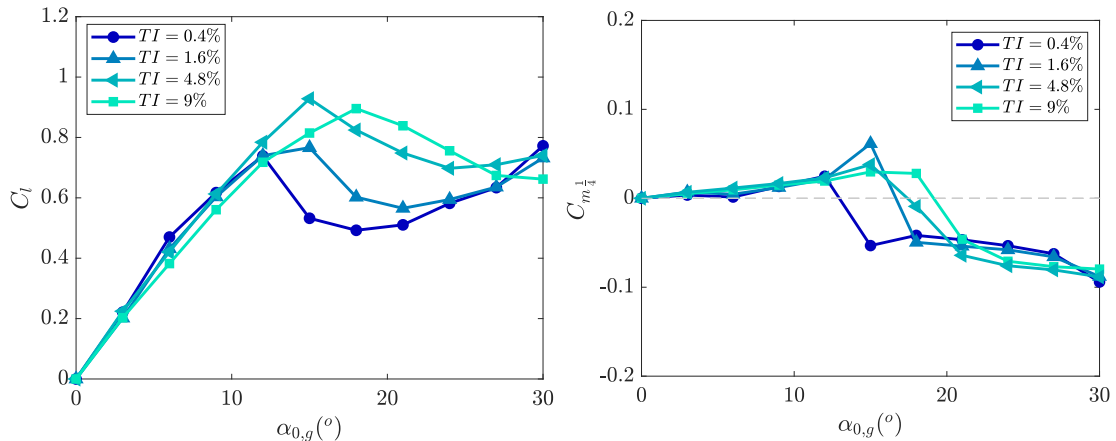
Figure 3.1: Lift coefficient C_l and moment coefficient at the quarter chord $C_{m\frac{1}{4}}$ as functions of geometric angle of attack $\alpha_{0,g}$ for $U_\infty = 25\,\text{m/s}$.

1.2 Spectra of far-field acoustic pressure with respect to the airfoil incidence

The power spectral densities (PSD) of far-field acoustic pressure at microphone M_{90} are presented in Figure 3.2a in the case without turbulence grid, with and without tripping. For a small incidence ($\alpha_{0,g} = 3°$) without tripping, the presence of tonal noise is visible for frequencies above $1000\,\text{Hz}$. It is composed of a fundamental frequency of $1530\,\text{Hz}$ and its harmonics. This spectral shape is characteristic of trailing edge noise associated to a laminar boundary layer [13, 9]. Paterson *et al.* [14] show that the evolution of the fundamental frequency with the inflow velocity follows a ladder-type structure with a main slope of $U^{1.5}$ and ladders of slope $U^{0.8}$. Just after the stall angle ($\alpha_{0,g} = 15°$), the tonal noise is found to disappear, and a strong broadband increase of the noise is observed below $700\,\text{Hz}$. At the extreme value of $30°$, a strong peak emerges around $84\,\text{Hz}$, as noticed by Moreau *et al.* [2]. This is associated to the vortex shedding frequency commonly observed downstream of a bluff body, as will be shown in more details in Section 2.

As the Reynolds number is much higher on wind turbine blades, the presence of laminar boundary layer trailing edge noise if very unlikely, and we add tripping on both sides of the airfoil to remove it, as can be seen in Figure 3.2b. At $\alpha_{0,g} = 3°$, the broadband noise between $300\,\text{Hz}$ and $2000\,\text{Hz}$ thus corresponds to turbulent boundary layer trailing edge noise, that is only a few decibels above the background noise. After stall, the spectra with and without tripping appear very close, due to the fact that the tripping tape has a small influence on the airfoil aerodynamics.

We now study the influence of the turbulence intensity on far-field noise in Figure 3.3. For $TI = 1.6\%$, a significant noise increase is observed at $\alpha_{0,g} = 3°$, that can be associated to turbulence interaction noise (also called leading edge noise). The effect is less important at higher angles of attack. For $TI = 4.8\%$, on the other hand, the PSDs are

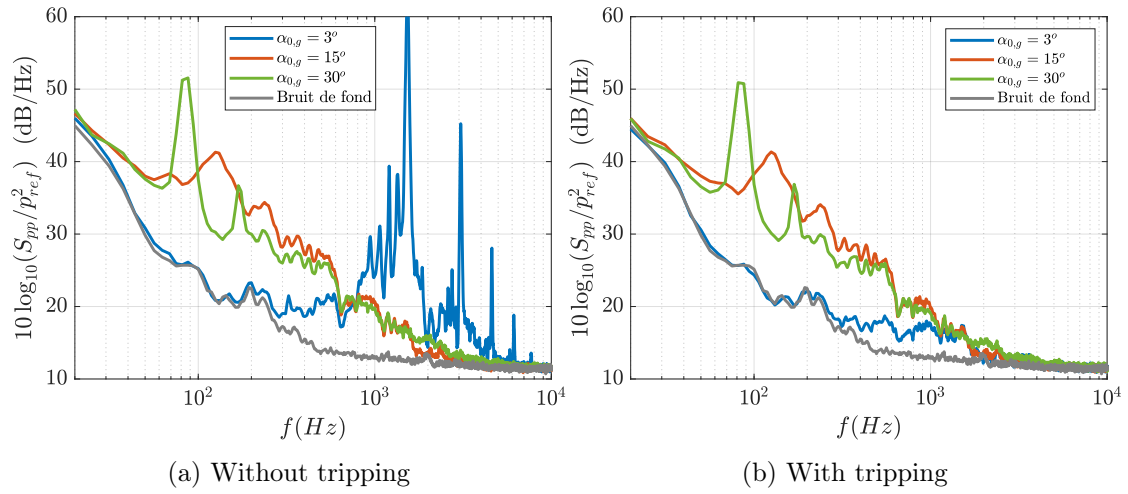(a) Without tripping   (b) With tripping

Figure 3.2: Power spectral density of acoustic pressure at microphone M_{90} without turbulence grid and (a) without tripping or (b) with tripping.
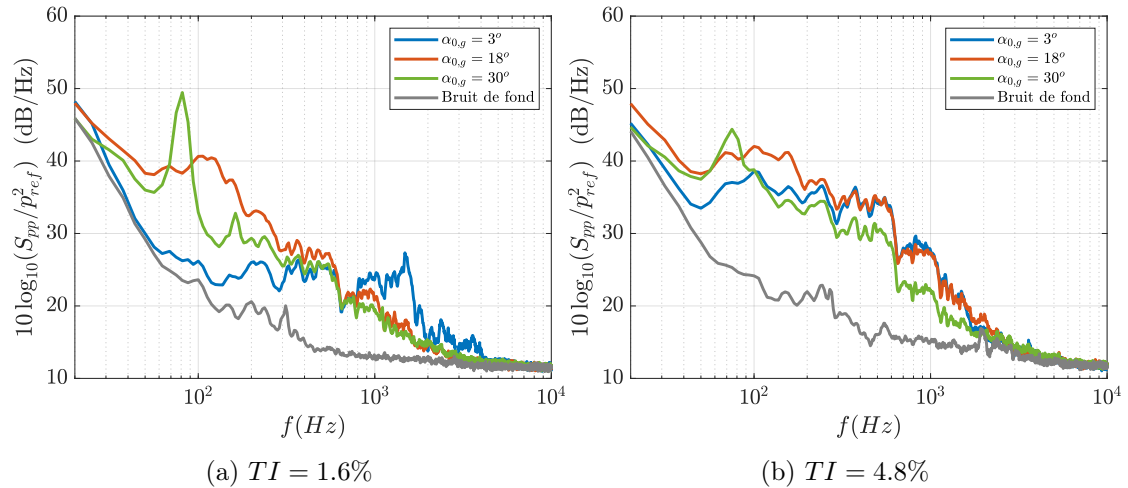

(a) $TI = 1.6\%$ (b) $TI = 4.8\%$

Figure 3.3: Power spectral density of acoustic pressure at microphone M_{90} with (a) $TI = 1.6\%$ or (b) $TI = 4.8\%$.

strongly modified for all angles of attack, with a strong broadband noise between 50 Hz and 2000 Hz. This means that turbulence interaction noise is the dominant mechanism here. At $\alpha_{0,g} = 30°$, the peak around 84 Hz is still visible but with a reduced amplitude. This can be explained by Figure 3.1, who showed that increasing the turbulence intensity yields a stall delay and a milder drop of the lift coefficient.

1.3 Noise radiated by an oscillating airfoil without tripping

To emphasize the importance of the tripping tape, we study here the noise radiation by the airfoil in the regimes $\alpha_g(t) = 5° + 7° \sin(2\pi f_0 t)$ and $\alpha_g(t) = 15° + 7° \sin(2\pi f_0 t)$, without turbulence grid and without tripping. The inflow velocity is $25\,\mathrm{m/s}$. The spectrograms are phase-averaged over 90 oscillations and are plotted in Figure 3.4. In the regime $\alpha_g(t) = 5° + 7° \sin(2\pi f_0 t)$, tonal peaks are clearly present between $1000\,\mathrm{Hz}$ and $3000\,\mathrm{Hz}$. This corresponds to the laminar boundary layer trailing edge noise seen previously in static conditions, that also takes place in the dynamic regime. It will be seen in Section 2 that this noise is again removed when tripping is added. In the regime $\alpha_g(t) = 15° + 7° \sin(2\pi f_0 t)$, we reach higher angles of attack and stall noise emerges at low frequencies. At low angles of attack, tonal peaks can still be observed, though at a smaller amplitude.
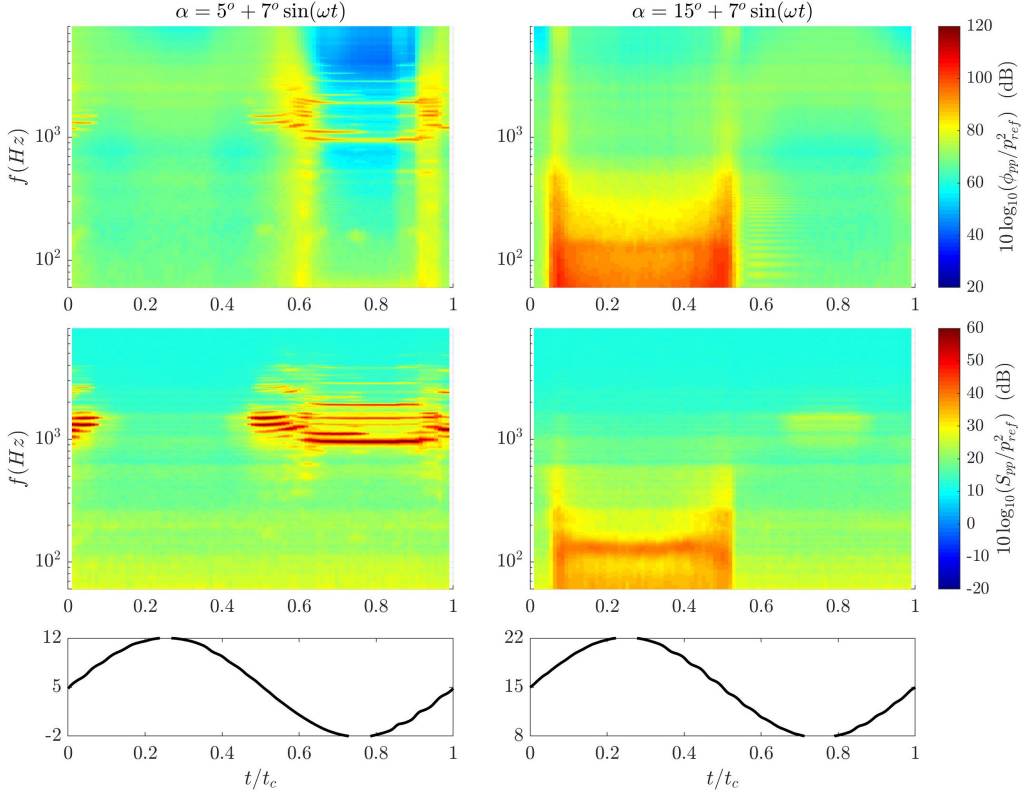
Figure 3.4: Phase-averaged spectrograms without grid and without tripping. The first line corresponds to the PSD of wall pressure at $x/c = 0.92$ on the suction side, the second line to the PSD of acoustic pressure at microphone M90, and the third line to the evolution of the angle of attack. The time t is made non-dimensional using the duration of one cycle $t_c = 1/f_0$.

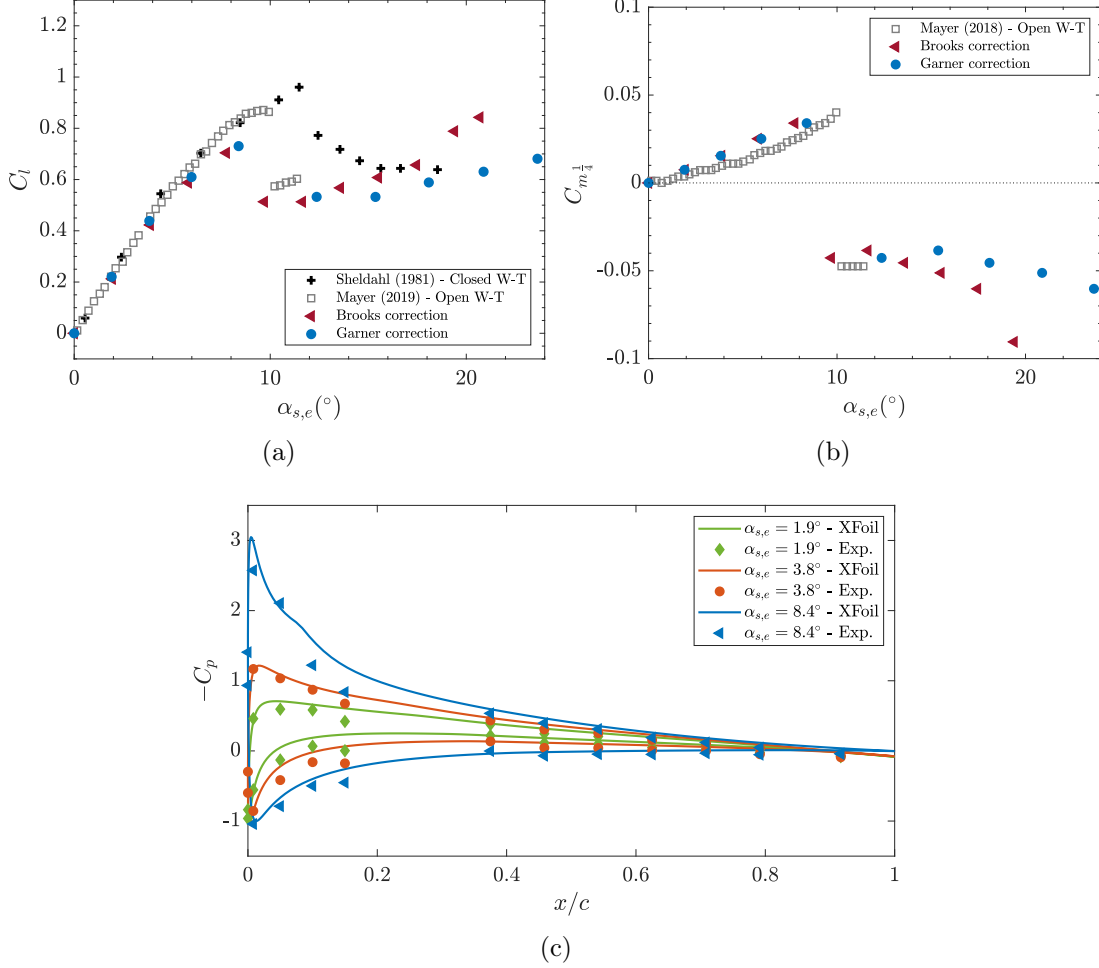# 2 Static airfoil stall noise without turbulence grid and with tripping

(a)

(b)

(c)

Figure 3.5: Comparison of the (a) lift coefficient and (b) moment coefficient at the quarter chord as functions of the effective static angle of attack $\alpha_{s,e}$ calculated with corrections by [15] and [16]. Open wind tunnel data of [17] are corrected with Brooks' correction, with $\eta = 1.73$. (c) Comparison of static pressure distribution $-C_p$ between experiments and XFoil simulations for effective angles of attack estimated with Garner corrections.

We now perform a detailed analysis of the aerodynamics and broadband noise radiation of the static airfoil at $U_\infty = 25\,\text{m/s}$ without turbulence grid and with tripping. The lift coefficient C_l and the moment coefficient at the quarter chord $C_{m\frac{1}{4}}$ are estimated by integrating the steady surface pressure along the airfoil chord and are presented in Figure 3.5. The static stall angle α_{ss} is identified as the angle of lift drop and sign inversion of the moment coefficient. The 3 degrees increment between static angle measurements

cannot allow a precise estimate of the static stall angle. The static stall angle is predicted between $\alpha_{s,e} = 7.7°$ and $\alpha_{s,e} = 9.7°$ with the correction from Brooks *et al.* [15], while it is predicted between $\alpha_{s,e} = 8.4°$ and $\alpha_{s,e} = 12.4°$ with the correction from Garner *et al.* [16]. The small values obtained with Brooks'correction reflect the fact that this correction is not accurate for high angles of attack. Comparisons with the lift coefficients obtained with a NACA0012 in another open wind-tunnel at $Re_c = 4.0 \times 10^5$ (see Ref. [17]) and in a closed wind-tunnel at $Re_c = 3.6 \times 10^5$ (see Ref. [18]) show a good quantitative agreement with current results, confirming that the maximum lift coefficient $C_{l,\text{max}}^{\text{static}}$ obtained in an open wind-tunnel is lower than unity. Further validation of the angle of attack corrections is performed by comparing the measured distribution of static pressure coefficient C_p along the airfoil chord with XFoil simulations. Figure 3.5(c) shows an overall good agreement between experiments and XFoil simulations for effective angles of attack estimated thanks to Garner corrections.

Figure 3.6 show the evolution of the PSD of the far-field sound pressure S_{pp} and the PSD of the airfoil surface pressure fluctuations ϕ_{pp} at $x/c = 0.92$ on the suction side for various static angles of attack $\alpha_{s,g}$. For the far-field noise, Figure 3.6(a) shows the raw PSD of the sound pressure while Figure 3.6(b) presents the PSD of far-field sound pressure with background noise substracted and data discarded if the total noise does not exceed the background noise by at least 2 dB. For $\alpha_{s,g} = 3°$, the attached turbulent boundary-layer trailing-edge noise is observed: the sound spectrum displays a broadband behavior between 300 Hz and 2000 Hz while the surface pressure PSD is flat with a slight hump centered at 2.5 kHz. The signal to noise ratio is low, with background noise dominating below 300 Hz and above 2 kHz. The increase of the surface pressure PSD at low frequency ($f < 70$ Hz) might be due to a contamination of the spectra by the background noise. For an angle close to stall ($\alpha_{s,g} = 12°$), the far-field noise is increased ($+4.5$ dB at 500 Hz in comparison with $\alpha_{s,g} = 3°$), which can be attributed to a flow separation on the suction side of the airfoil. This assumption is confirmed by the increase of the amplitude of surface pressure PSD for low frequencies ($f < 2000$ Hz) and the shift of the maximum to a lower frequency ($f = 600$ Hz), indicating an increase of the boundary layer thickness. It is interesting to note that, in spite of the amplitude change, the frequency ranges of the far-field noise for $\alpha_{s,g} = 3°$ and $\alpha_{s,g} = 12°$ are similar.

For the stalled configurations, two regimes are visible, corresponding to the so-called "light-stall" and "deep-stall" regimes [2]. In the light-stall regime ($\alpha_{s,g} = 15°$), a broadband noise is observed between 50 Hz and 700 Hz, with a significant increase at low frequencies ($+15$ dB at 250 Hz, in comparison with $\alpha_{s,g} = 12°$). The surface pressure PSD exhibits a higher energy content in the low frequencies ($f < 1000$ Hz) than before stall. This high energy in the low frequency range suggests that larger structures are present on the suction side of the airfoil compared to the attached-flow configuration.

The deep-stall regime ($\alpha_{s,g} = 27°$) is characterized by a broadband noise of lower amplitude and a narrow-band peak at 96 Hz. Noise spectra for other high angles of attack not shown here ($\alpha_{s,g} \geq 18°$) all exhibit a peak at $St = 0.21$, where $St = fc\sin(\alpha_{s,g})/U$ is the Strouhal number based on the apparent frontal width of the airfoil. This peak, also noticed on the surface pressure PSD, can be explained by shear layer instabilities
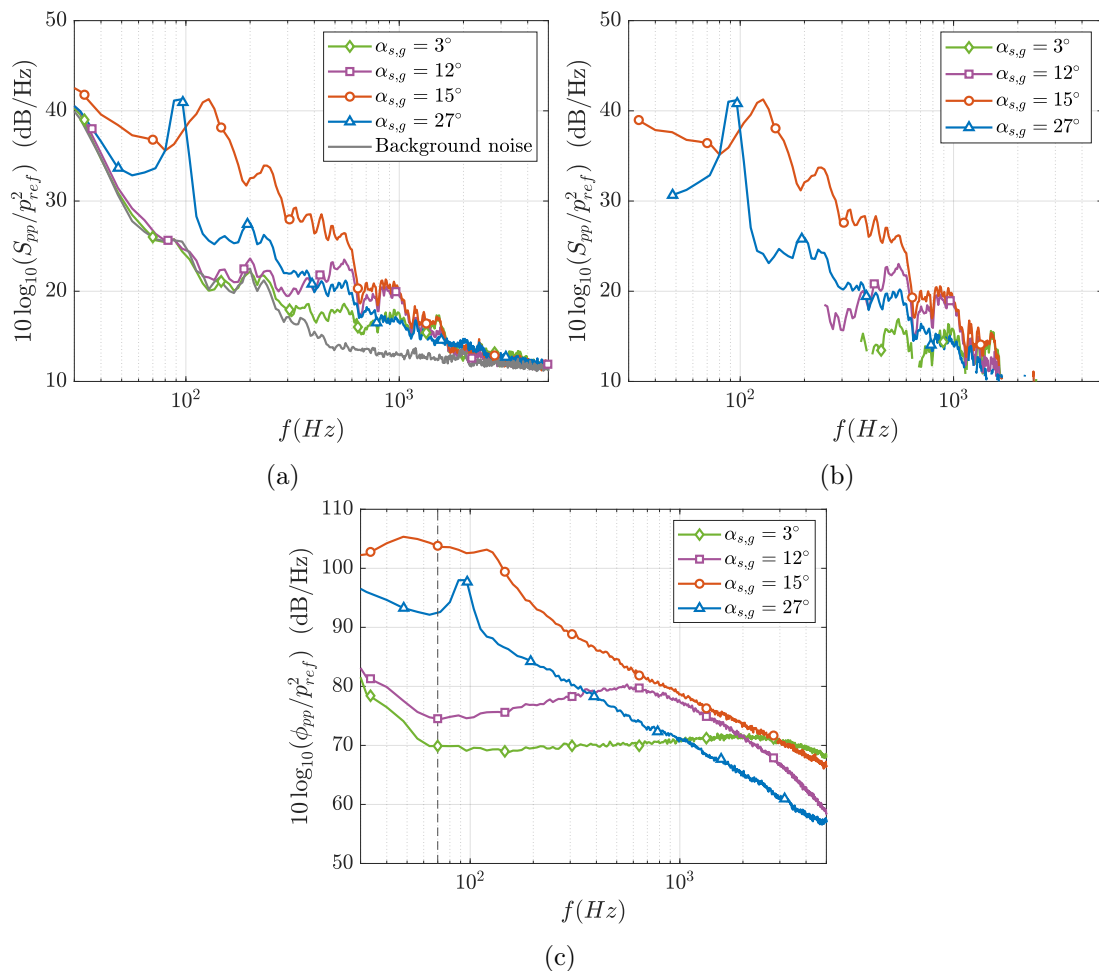
23

(a)

(b)

(c)

Figure 3.6: PSD of the far-field acoustic pressure for various static angles of attack: (a) raw spectra (b) with background noise substracted and data discarded if the total noise does not exceeds the background noise by at least 2 dB. (c) PSD of the surface pressure fluctuations at $x/c = 0.92$ on the suction side of the airfoil, for various static angles of attack. The vertical dashed black line shows the limit below which the surface pressure spectra is thought to be contaminated by the wind tunnel background noise.

and large-scale periodic vortex shedding [2]. At frequencies below and above this peak, the deep-stall regime is less noisy than the light-stall regime, in good agreement with observations by Laratro *et al.* [10]. Similarly, the surface pressure spectrum level is lower in the deep-stall regime than in the light-stall regime on the entire frequency range.

For a fully attached boundary layer, the noise is generated at the trailing-edge of the airfoil [13, 19]. In the framework of Amiet's theory, the far-field acoustic pressure PSD S_{pp} is proportional to the surface pressure PSD ϕ_{pp} at the trailing edge and to the spanwise correlation length l_y [19, 20]. As the flow starts separating, the trailing edge

(a) $\alpha_{s,g} = 3°$ ($\alpha_{s,e} = 1.9°$)

(b) $\alpha_{s,g} = 12°$ ($\alpha_{s,e} = 8.4°$)

(c) $\alpha_{s,g} = 15°$ ($\alpha_{s,e} = 12.4°$)

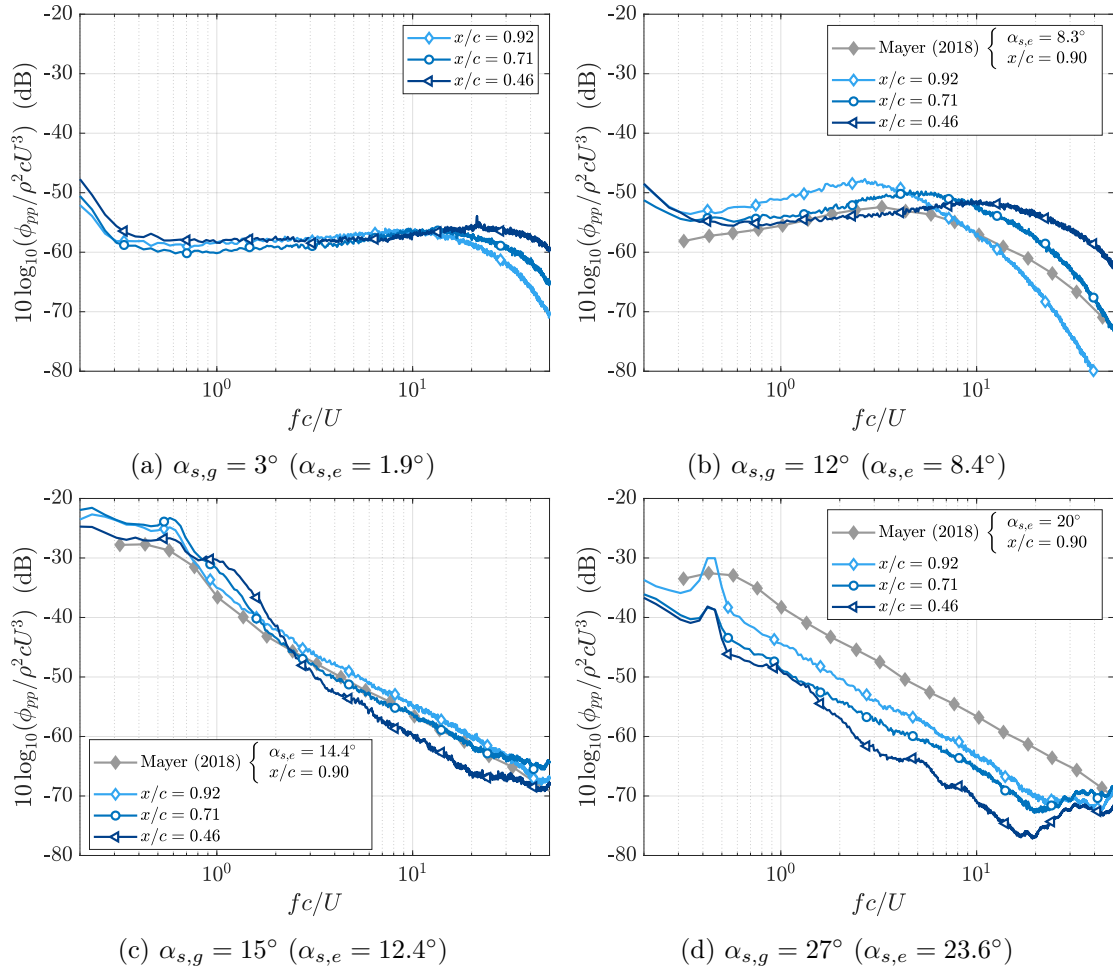(d) $\alpha_{s,g} = 27°$ ($\alpha_{s,e} = 23.6°$)

Figure 3.7: Surface pressure PSD for three positions along the airfoil chord, and for various static angles of attack.

is still found to be the main source of noise [2, 4]. Surface pressure PSD measured at different positions along the chord are shown in Figure 3.7, for various static angles of attack. For comparison with the measurements by Mayer *et al.* [17] in a closed wind tunnel at $Re = 4 \times 10^5$, the spectra are normalized by $\rho^2 c U^3$, as suggested by Bertagnolio *et al.* [3]. For an attached boundary layer ($\alpha_{s,g} = 3°$), similar surface pressure PSD are obtained for the 3 positions along the chord, with a plateau for $1 < fc/U < 3$. However, as the flow separates ($\alpha_{s,g} = 12°$), differences are obvious between the three chord positions. At $x/c = 0.46$, the spectrum still exhibits a plateau with a slight hump at $fc/U = 1$. For positions closer to the trailing-edge, the plateau disappears and the hump amplitude increases while shifting to lower frequencies (at $fc/U = 6$ for $x/c = 0.71$ and at $fc/U = 2.5$ for $x/c = 0.92$). For the light stall regime ($\alpha_{s,g} = 15°$), three regions can be spotted. For $fc/U < 0.8$ and $fc/U > 3$, the surface pressure PSD is higher closer to the trailing edge. On the other hand, for $0.8 < fc/U < 3$ Hz, the spectral levels are higher closer to the center chord $x/c = 0.46$. Finally, for the deep stall regime ($\alpha_{s,g} = 27°$), the surface pressure PSD is always maximum close to the trailing edge. A good agreement is obtained with closed wind tunnel experiment at $Re = 4 \times 10^5$ [21], the spectra exhibiting similar slopes in the post-stall regimes. The poor magnitude agreement observed in Figure 3.7(d) could be explained by the simplistic normalizing used here and/or by the difference in Reynolds number and angle of attack between the two experimental conditions. According to Bertagnolio *et al.* [3], using the chord-wise correlation length L_x instead of the chord c could lead to a better collapse of the data. Using a normalized frequency $f x_{RMP}/U$, with x_{RMP} being the surface pressure probe location, was tested and did not lead to a better collapse of the surface pressure PSD hump center frequencies.

As the surface pressure spectra exhibit close behaviors for the three chord positions and as the amplitude of the surface pressure spectrum is maximum near the trailing edge for the stall condition, only the surface pressure at $x/c = 0.92$ is shown in the following.

3 Oscillating-airfoil stall noise without turbulence grid and with tripping

3.1 Time-frequency analysis

For the oscillating airfoil regimes, a time-frequency analysis is first performed in order to observe how the surface pressure and far-field noise spectra vary during the oscillation. The spectrograms of the surface pressure and far-field noise for $\alpha_{d,g} = 15° + 7° \sin(2\pi f_o t)$ and $k = 0.02$ are plotted in Figure 3.8. The far-field noise and surface pressure fluctuations exhibit strong amplitude variations within an oscillation period. Moreover, the signals of the surface pressure and noise appear to be periodic and strongly in-phase with the instantaneous angle of attack of the airfoil. High values of the angle of attack are associated with a low-frequency noise contribution. Meanwhile, a high-energy content region appears on the surface pressure spectrogram, with amplitude increases up to +40 dB compared to the attached flow stages.
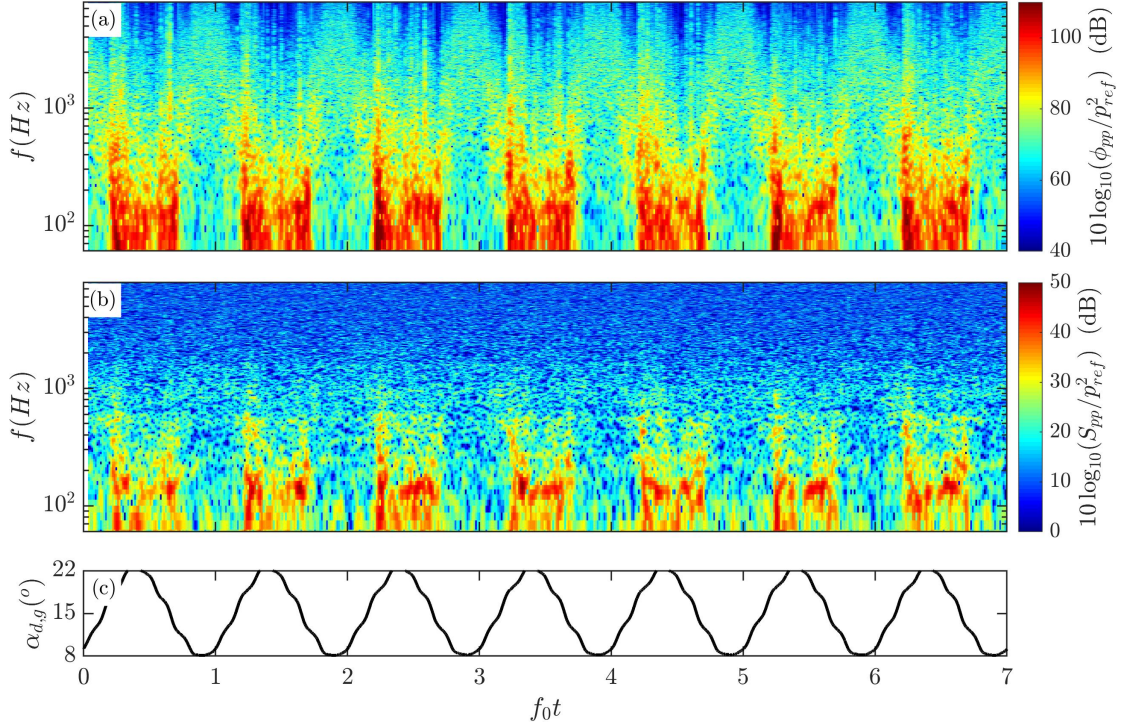
Figure 3.8: Spectrograms of (a) surface pressure fluctuations at $x/c = 0.92$ (b) far-field acoustic pressure and (c) instantaneous geometric angle of attack $\alpha_{d,g} = 15° + 7° \sin(2\pi f_o t)$ with $k = 0.02$ ($k_\star = 2.4 \times 10^{-3}$).

The spectral content during the stalled stage of the cycle is not uniform. At the stall onset, both the far-field noise and surface pressure present a region of high energy at frequencies up to 1 kHz for a short time interval, whereas the contribution of the remaining part of the stalled stage is limited to frequencies below 1 kHz. As for the static case, the stalled phase exhibits a decrease of the surface pressure level at high frequencies ($f > 1$ kHz) compared to the attached phase, in good agreement with surface pressure spectrograms obtained by Mayer *et al.* [6] at $x/c = 0.90$. No variations of the far-field noise are visible for $f > 1$ kHz, the frequency range of this quasi-steady stall regime noise is thus similar to the frequency range of the static stall noise.

As results for other oscillation frequencies and amplitudes all exhibit this periodic behavior of far-field noise and surface pressure with respect to the angle of attack, it is possible to apply phase-averaging to microphones and angle of attack signals. Figures 3.9 and 3.10 present the phase-averaged spectrograms for the six oscillating airfoil regimes. In all the following, the overbar denotes phase-averaging. Note on Figure 3.9 (g-h-i) and Figure 3.10 (g-h-i) that the motion of the airfoil imposed by the motor is not a perfect sine function. Slight oscillations are evidenced; they are not believed to be prejudicial

27

for the present time-frequency analysis.

For the quasi-steady regime $\alpha_1 = 7°$ and $k = 0.01$ (left column of Figure 3.9), no variation of the noise level is visible outside the stalled stage of the cycle. During the stalled stage, the far-field noise spectrogram is nearly symmetrical. At the onset of stall ($f_0 t \sim 0.30$) and at the flow reattachment time ($f_0 t \sim 0.78$), broadband noise is emitted between 70 Hz and 700 Hz. Between these two moments, the acoustic energy is concentrated in a narrow-band peak centered around $f \simeq 140$ Hz. The light and deep stall regimes observed for a static airfoil are thus still present for an oscillating airfoil in a quasi-steady stall configuration. As for the far-field noise, the surface pressure spectra contain energy at higher frequencies at the stall onset and before flow reattachment than during the stalled stage.

For $\alpha_1 = 15°$ and $k = 0.01$, nearly symmetrical spectrograms are also obtained during the stalled stage for the surface pressure and far-field noise, as seen on the left column of Figure 3.10. For this regime, the range of angles of attack during the stalled stage is higher than for $\alpha_1 = 7°$, leading to a visible shift of the narrow-band peak frequency over time on the far-field noise. Just after the stall onset, the narrow-band peak is centered around $f \simeq 145$ Hz. As the angle of attack increases, the center frequency of the peak decreases until reaching a plateau at $f \simeq 94$ Hz, while the airfoil reaches its maximum incidence. The center frequency of the narrow-band peak then starts increasing as the angle of attack decreases, and ends up being centered at $f \simeq 145$ Hz just before the broadband noise at reattachment. This narrow-band peak frequency shift is in good agreement with the static airfoil results, with a Strouhal number $St = fc\sin(\overline{\alpha_{d,g}})/U \simeq 0.22$. During the quasi-steady stall regimes, the sizes of the large structures periodically shed in the flow continuously vary and adapt to the angle of attack of the airfoil. It is noteworthy that, even for the lower reduced frequency $k = 0.01$, the stalled phase is not centered around the maximum of the sinusoidal motion, but is slightly delayed. This phenomenon and the induced hysteresis are investigated in Section 3.2.

For $k = 0.02$, similar results are obtained (middle columns of Figures 3.9 and 3.10). However, the symmetrical behavior between stall onset and flow reattachment is lost, the broadband noise at stall onset extending to higher frequencies than the broadband noise at reattachment. This asymmetry is more pronounced for $k = 0.05$ with an increase of the width and amplitude of the stall onset broadband noise. For the dynamic stall regime $k = 0.05$ and $\alpha_1 = 15°$ (see Figure 3.10(f)), the stalled stage of the noise cycle does not exhibit any symmetry. The width and amplitude of the broadband noise at stall onset clearly increase, whereas the broadband noise at flow reattachment has a similar length and amplitude compared to the quasi-steady regimes.

3.2   Overall Sound Pressure Level

In order to further investigate the noise events observed in the spectograms, a temporal analysis of the dynamic stall noise is conducted by integrating the frequency content of
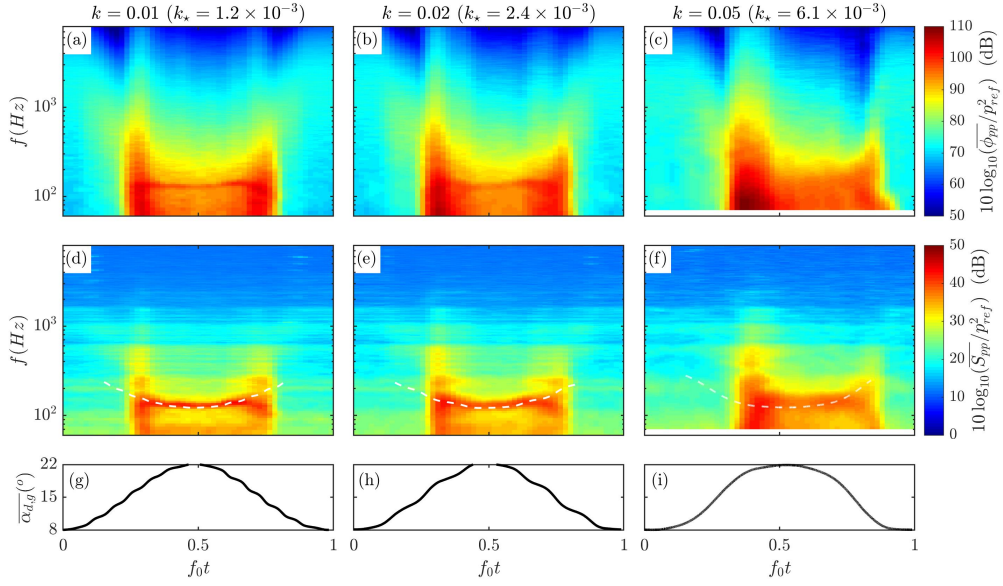
Figure 3.9: Phase-averaged spectrograms of (a-b-c) surface pressure fluctuations at $x/c = 0.92$ and (d-e-f) far-field sound pressure, for $\alpha_{d,g} = 15° + 7° \sin(2\pi f_o t)$ and various oscillation frequencies. The third line (g-h-i) shows the phase-averaged variations of angle of attack during one oscillation period. The overbar denotes phase-averaging. The white dashed lines show the evolution of the frequency f corresponding to a constant Strouhal number $St = fc \sin(\overline{\alpha_{d,g}})/U = 0.22$.
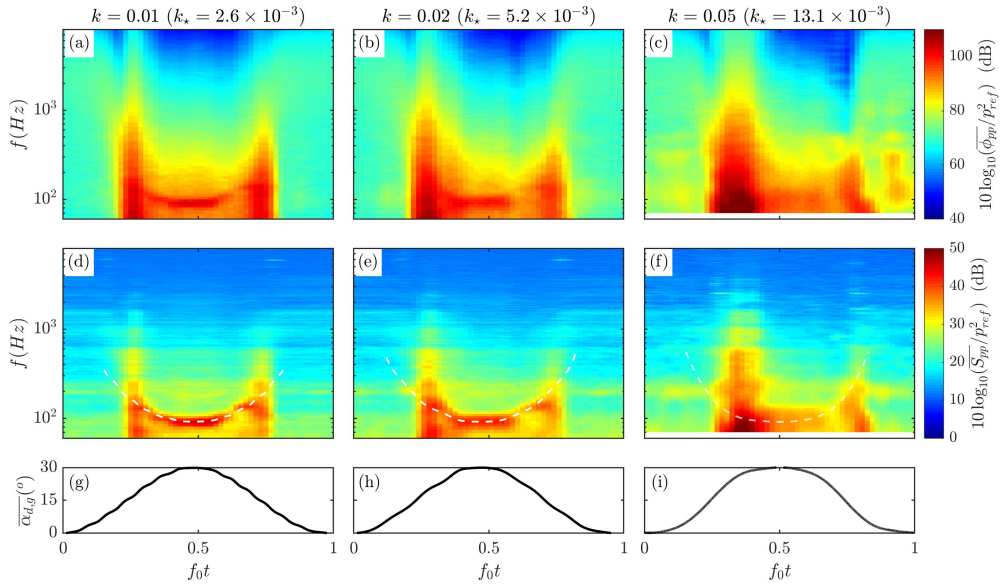
Figure 3.10: Same as Figure 3.9 with $\alpha_{d,g} = 15° + 15° \sin(2\pi f_o t)$.
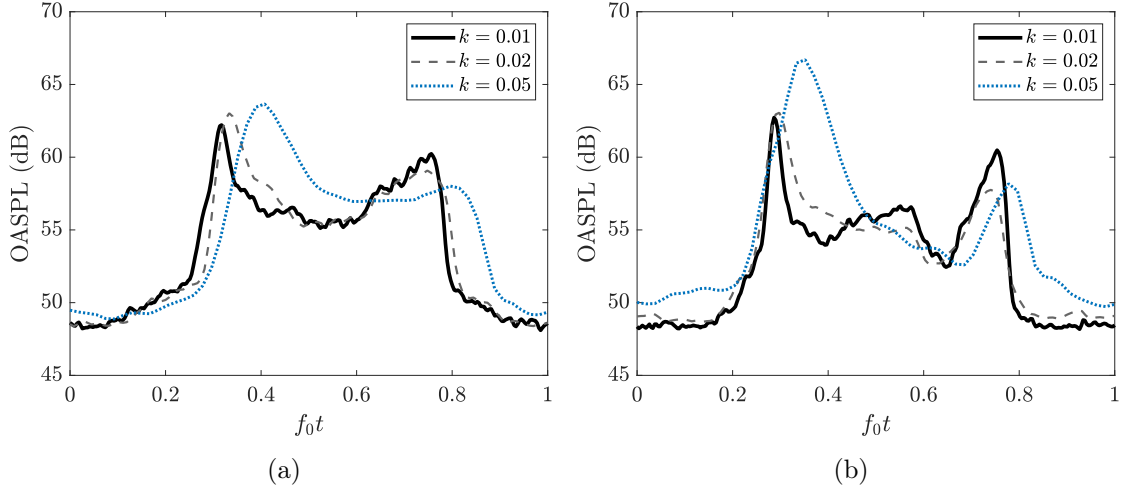
Figure 3.11: Phase-averaged OASPL plotted against time for $\alpha_{d,g} = 15° + 7° \sin(2\pi f_o t)$
.

the noise. The Overall Sound Pressure Level (OASPL) is defined as:

$$\text{OASPL} = 10 \log_{10} \left(\frac{1}{p_{ref}^2} \int_{f_1}^{f_2} S_{pp} df \right), \tag{3.1}$$

with $p_{\text{ref}} = 20\mu$Pa a reference pressure and $f_1 = 70$ Hz and $f_2 = 1000$ Hz. These values are chosen in order to capture the noise amplitude variations in the stall noise frequency range, as measured in static (Figure 3.6) and dynamic (Figures 3.9 and 3.10) configurations, while minimizing the effect of background noise.

The phase-averaged OASPL is plotted against time in Figure 3.11, $f_0 t = 0$ corresponding to the minimum value of $\alpha_{d,g}$. The stalled stage of the noise cycle is characterized by an increase of the noise amplitude by 5 to 15 dB approximately, compared to the attached flow stage. For all the regimes studied here, the OASPL first reaches a maximum value $\text{OASPL}_{\text{max}}$ close to the stall onset. It then decreases and reaches a plateau, corresponding to the dynamic deep stall stage observed in Figures 3.9 and 3.10. Finally, the OASPL increases and reaches a second local maximum, marking the onset of flow reattachment, followed by a rapid decrease. For $k = 0.01$, the two local maxima of OASPL have nearly the same value, confirming the aforementioned symmetry, while for higher reduced frequencies, they significantly differ. The value of the stall maximum $\text{OASPL}_{\text{max}}$ strongly increases and the value of the reattachment local maximum slightly decreases compared to the case $k = 0.01$.

In order to compare the aerodynamics of the airfoil and the emitted far-field noise, the OASPL and lift coefficient are both plotted against the angle of attack in Figure 3.12 for the static and oscillating airfoil regimes. Note that the static curves are the same and can be used as references for the six dynamic stall experiments. As explained in Section 2, steady pressure taps are mainly distributed on one side of the airfoil. In order
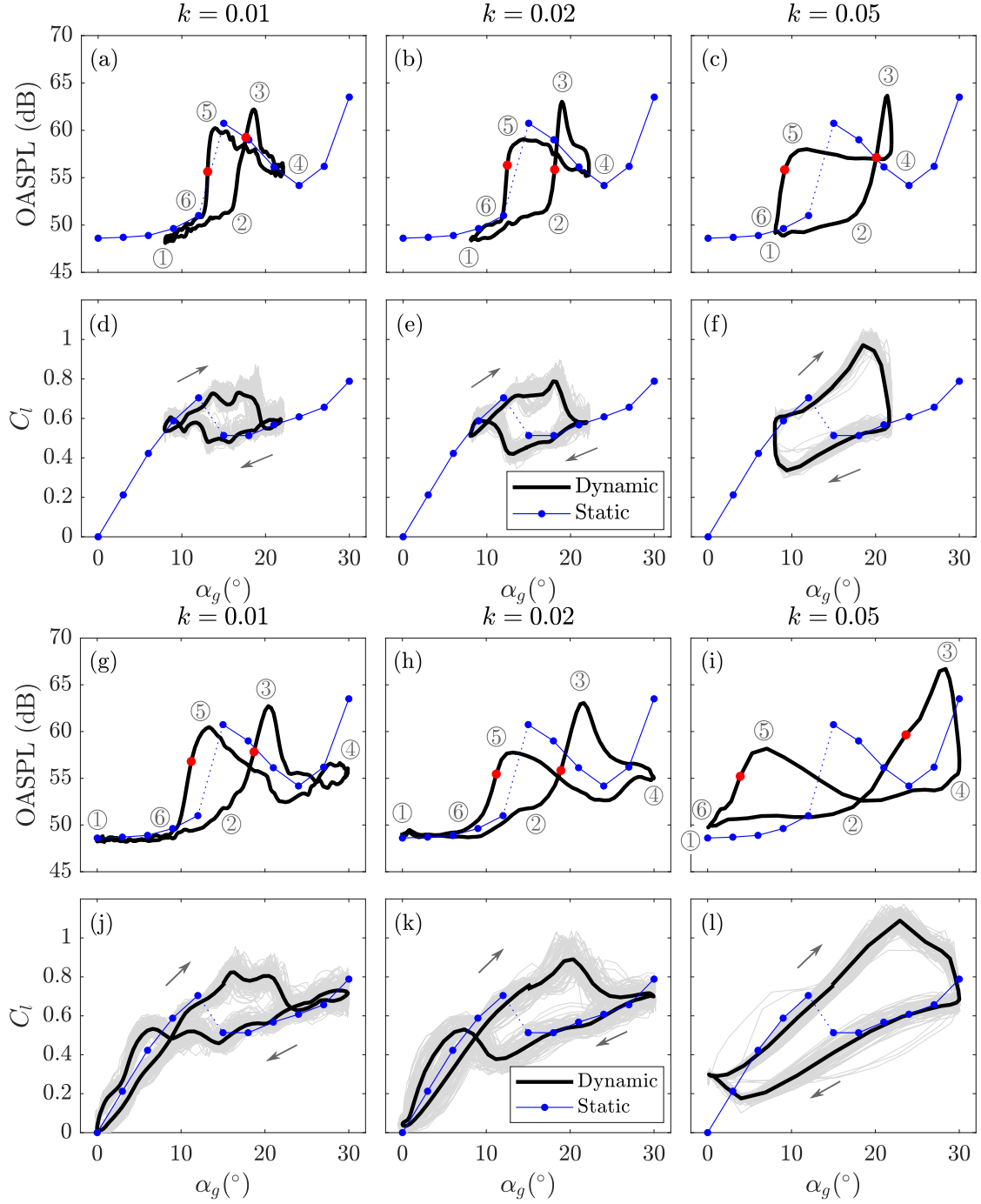
30

Figure 3.12: Phase-averaged OASPL and lift coefficient C_l versus the angle of attack for (a-f) $\alpha_{d,g} = 15° + 7° \sin(2\pi f_o t)$ (g-l) $\alpha_{d,g} = 15° + 15° \sin(2\pi f_o t)$. Grey lines show the instantaneous lift coefficient. Red dots show the angle of maximum $d\text{OASPL}/dt$. α_g here denotes the static or dynamic geometrical angle of attack. Events are defined as: ① Minimum of OASPL and angle of attack, ② Onset of fast OASPL increase, ③ Maximum of OASPL, ④ Maximum of angle of attack, ⑤ Second local maximum of OASPL during downstroke motion and ⑥ End of the rapid OASPL decrease.

to calculate C_l for dynamic regimes by integrating the steady pressure along the airfoil, it is therefore necessary to perform measurements for both $\alpha_{d,g} = \alpha_0 + \alpha_1 \sin(2\pi f_o t)$ and $\alpha_{d,g} = -\alpha_0 + \alpha_1 \sin(2\pi f_o t)$, and synchronize the pressure taps during the post-processing phase. This synchronization is a source of error in the estimation of C_l. Moreover, the fact that the motor is not able to generate a perfect sinusoidal motion is also visible on the lift coefficient curves, with slight lift oscillations added to the main lift curve, as seen for example in Figures 3.12(d) and 3.12(j). Again, this artifact is not pronounced enough to question the global analysis of the cycle. The dynamic lift coefficients C_l presented in Figure 3.12 have thus to be considered as estimates of the real lift coefficients, with some uncertainty.

Characteristic noise events of the quasi-steady and dynamic stall cycles are numbered from ① to ⑥ and defined in the caption of Figure 3.12. Similar noise patterns are obtained for the quasi-steady regimes $k \leq 0.02$, for both $\alpha_1 = 7°$ and $15°$. Starting at position ①, the flow is attached and the OASPL for the oscillating airfoil is equal to the one for a static airfoil at the same angle of attack. From position ① to position ②, the angle of attack increases until exceeding the static stall angle but the flow remains attached, the lift coefficient C_l exceeding its maximum static value. From positions ② to ③, the OASPL rapidly increases by more than 10 dB for all the investigated regimes, marking the stall noise radiation, until reaching the maximum OASPL at position ③. Between these two positions, the lift coefficient C_l first reaches its maximum $C_{l,\max}$, before rapidly decreasing. Between positions ③ and ⑤ the flow is fully stalled. A decrease of the OASPL is first visible between positions ③ and ④, as the angle of attack keeps on increasing above the dynamic stall angle. As the angle of attack starts decreasing, the OASPL increases again until reaching a local maximum at position ⑤. The flow reattachment takes place between positions ⑤ and ⑥, where the OASPL decreases rapidly until reaching the static OASPL value at position ⑥. The angle of attack at the onset of the rapid OASPL increase (position ②) is different from the angle of attack at the rapid OASPL decrease (position ⑥). The hysteresis commonly observed on dynamic lift curves is thus also observed on the OASPL curves. The width of the hysteresis is increasing as the reduced frequency increases. For $k = 0.05$ and $\alpha_1 = 15°$, differences are visible on the OASPL and C_l curves. Unlike for lower oscillation frequencies, the lift coefficient is never decreasing down to $C_l = 0$ when the dynamic angle of attack is low. On the same way, the OASPL for the attached stage of the cycle (between positions ① and ②) is 2 dB higher than the OASPL at the same static angles of attack. For high reduced pitch rates, the trailing edge noise of an attached boundary layer is thus impacted by the pitching motion.

3.3 Frequency content of the noise events

Phase-averaged PSD of the far-field acoustic pressure and surface pressure at the characteristic events ① to ⑤ are extracted from spectrograms and presented in Figure 3.13, for $\alpha_{d,g} = 15° + 7° \sin(2\pi f_o t)$. The upward-pointing arrow (↑) indicates the upstroke motion of the airfoil while the downward-pointing arrow (↓) indicates the downstroke motion of the airfoil. Phase-averaged spectra at position ⑥ are not presented in Figure 3.13, as

32

they are close to the ones at position ②. Results for $\alpha_{d,g} = 15° + 15° \sin(2\pi f_o t)$ are not shown because they are similar to the ones presented here for $\alpha_{d,g} = 15° + 7° \sin(2\pi f_o t)$.

Starting at $\alpha_{d,g}(t) = 8°$ (position ①) for $k = 0.01$, the far-field noise spectra of Figures 3.13(a) and 3.13(b) display a low amplitude broadband behavior between 300 Hz and 2 kHz. In contrast the surface pressure spectrum is flat with a hump at 2 kHz, as for the trailing-edge noise observed for the static configuration for low angles of attack. As the upstroke motion starts and position ② is reached ($\alpha_{d,g}(t) = 16°(\uparrow)$), the amplitudes of the far-field and surface pressure spectra increase at low frequencies, because the boundary layer is separating on the suction side of the airfoil. This increase continues until reaching the light-stall regime $\alpha_{d,g}(t) = 18.45°(\uparrow)$, corresponding to the angle of maximum OASPL (position ③). As the upstroke motion continues and the maximum incidence is reached ($\alpha_{d,g}(t) = 22°$), a deep-stall type regime is observed, with an overall reduction of the broadband noise and the presence of a peak at $f = 125$ Hz, corresponding to a Strouhal number $St = fc\sin(\alpha_{d,g})/U = 0.22$. The downstroke motion leads to a second light-stall regime at $\alpha_{d,g}(t) = 13.9°(\downarrow)$ (position ⑤). This second light-stall regime is characterized by a broadband noise between 70 Hz and 700 Hz, with lower levels compared to the upstroke light-stall noise from position ③. Similarly, the surface pressure spectrum has a lower amplitude for the downstroke light-stall regime (position ⑤) than for the upstroke light-stall regime (position ③).

Similar results are obtained for $k = 0.02$ and $k = 0.05$ as can be seen in Figures 3.13(c) to 3.13(f). The main effect of increasing the reduced frequency k lays in the noise differences between the upstroke and the downstroke light-stall regimes. For $k = 0.01$, the noise levels in the upstroke and the downstroke light-stall regimes differ by less than 3 dB on the full stall noise frequency range. This difference increases as k increases, with the upstroke light-stall regime being up to 6 dB noisier than the downstroke light-stall regime for $k = 0.05$ (see Figure 3.13(f)). Present results do not allow us to investigate if large scale vortex shedding still takes place at $k = 0.05$, because the used window size is too small to study low-frequency narrow-peaks.

3.4   Comparison between the static and quasi-steady stall noise

A comparison between the quasi-steady stall noise and the static stall noise at similar angles of attack is now performed. Figure 3.14 presents the far-field PSD, surface-pressure PSD and steady pressure coefficient C_p distribution for the static regimes $\alpha_{s,g} = 12°$ (pre-stall), $\alpha_{s,g} = 15°$ (light-stall) and $\alpha_{s,g} = 21°$ (deep-stall), and for the dynamic regime $\alpha_{d,g} = 15° + 7° \sin(2\pi f_0 t)$ with $k = 0.01$. For a static airfoil, the light-stall noise is observed for $\alpha_{s,g} = 15°$. For the oscillating airfoil, the far-field noise spectrum at $\alpha_{d,g} = 15°(\uparrow)$ still exhibits a pre-stall type shape, with a low amplitude broadband noise limited to frequencies above 200 Hz. This delay of stall during the quasi-steady regime is confirmed by steady pressure measurements, with a steady pressure coefficient distribution similar for $\alpha_{d,g} = 15°(\uparrow)$ and for the static pre-stall regime $\alpha_{s,g} = 12°$ (see Figure 3.14(c)). On the other hand, during the downstroke motion, similar far-field and surface pressure spectra are obtained for the static airfoil at $\alpha_{s,g} = 15°$ and for the oscillating airfoil at $\alpha_{d,g} = 15°(\downarrow)$. This result confirms that a hysteresis is
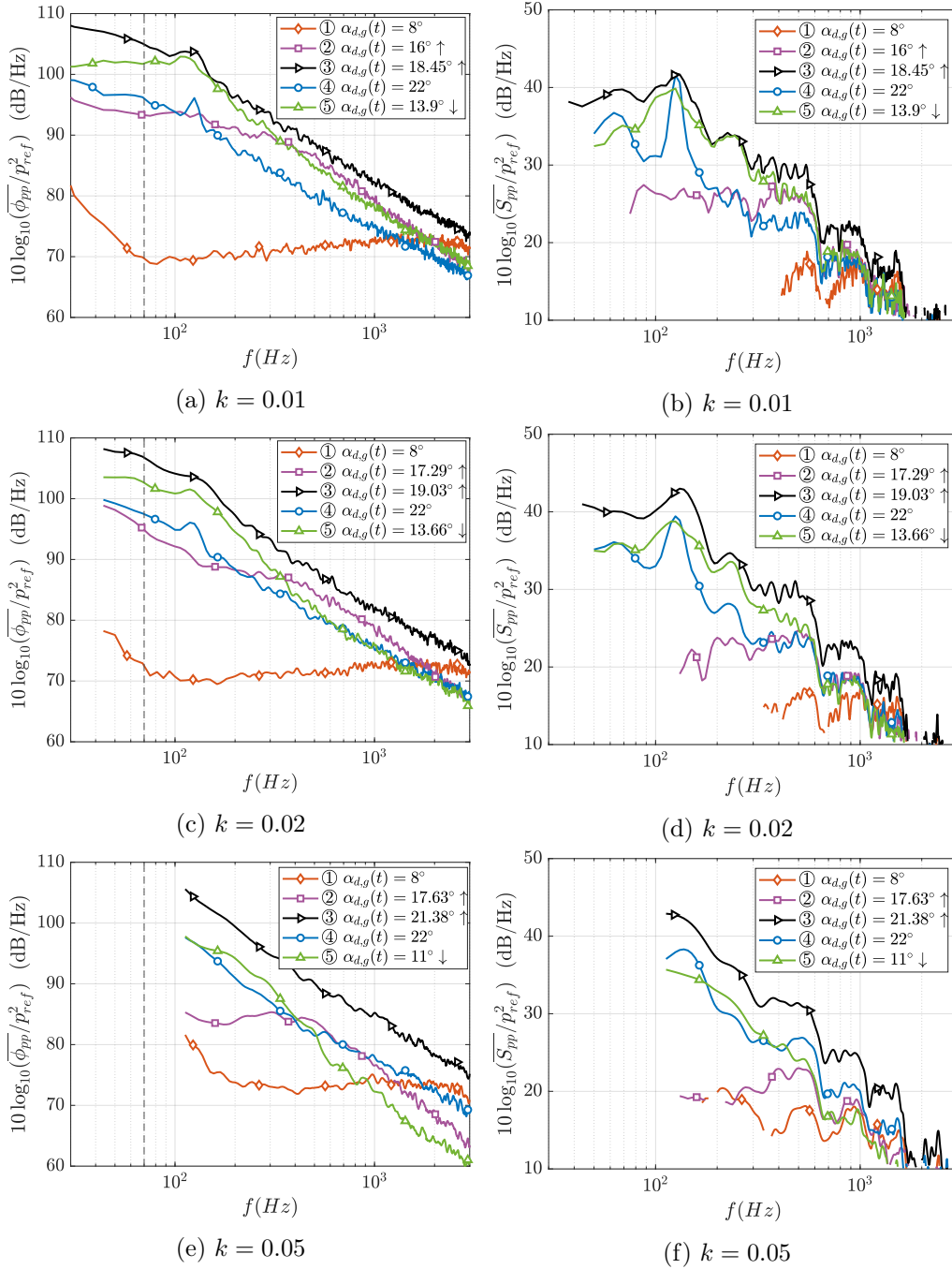
Figure 3.13: Phase-averaged PSD of (left column) surface pressure fluctuations at $x/c = 0.92$ and (right column) far-field acoustic pressure with background noise subtracted, during the noise events ① to ⑤ for $\alpha_{d,g} = 15° + 7° \sin(2\pi f_o t)$. The vertical dashed black line shows the limit below which the surface pressure spectra is thought to be contaminated by the wind tunnel background noise. Spectra are not displayed at frequencies when less than three points are present per spectrogram window.

34

present for the emitted noise, even for the quasi-steady regime with the lowest oscillation frequency investigated. The noise emitted by the quasi-steady oscillating airfoil can thus be predicted thanks to static noise measurements, and by adding an angle of attack delay that can be calculated using a dynamic stall model.

(a)

(b)

(c)

(d)
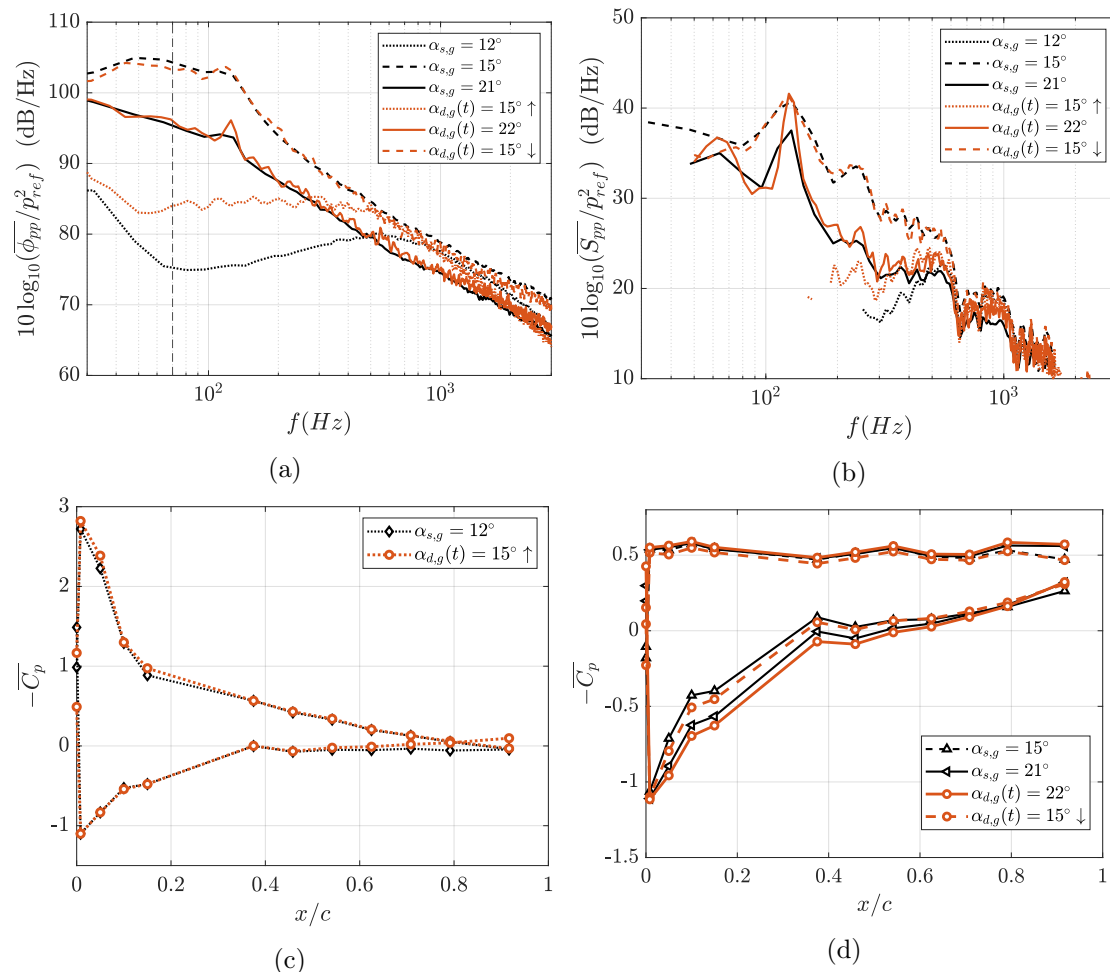
Figure 3.14: Comparison of phase-averaged (a) PSD of surface pressure fluctuations at $x/c = 0.92$, (b) PSD of far-field noise and (c-d) static pressure coefficient, between the static and the quasi-steady case $\alpha_{d,g} = 15° + 7° \sin(2\pi f_0 t)$ and $k = 0.01$. Background noise is substracted from far-field noise and data is discarded if the total noise does not exceeds the background noise by at least 2 dB.

Results of the second campaign using an instrumented NACA 63₃418 airfoil

In this chapter, results from the second campaign using a NACA 63_3418 airfoil are presented . First, the far-field noise spectra are characterized for a static airfoil in Section 1. Then, the influence of the oscillation frequency is studied in Section 2. Finally, the airfoil noise sources at high angles of attack in static conditions are identified in Section 1 using synchronous flow and acoustic measurements. Some of the results presented in this chapter are extracted from the article of Raus *et al.* [22] and from the PhD thesis of Lisa Sicard [23].

1 Mechanisms of noise generation on a static airfoil

In this section, we study both the case with tripping device on the pressure side without turbulence, called hereafter with tripping, and the case with turbulence grid ($TI = 1.6\%$,) and no tripping device, called hereafter with grid. All three incoming velocities are examined.

We consider first the evolution of the lift coefficient with respect to the angle of attack α_g, plotted in Figure 4.1 in the cases with tripping and with grid for the three incoming velocities. The curves are almost identical up to approximately $14°$, close to the static stall angle. In the case with tripping, the maximum lift coefficient varies slightly with respect to Reynolds number, and the lift sudden drop associated with the complete detachment of the boundary layer occurs at different angles of attack between $22°$ and $25°$. In the case with grid, on the other hand, the three curves overlap almost perfectly.

The power spectral density (PSD) of acoustic pressure at microphone 7 ($\theta = 90°$) is plotted in Figure 4.2 for various incidence angles at $U = 50\,\mathrm{m/s}$. In the case with tripping, the spectrum at $\alpha_g = 2°$ is close to the background noise, with a significant signal to noise ratio between $800\,\mathrm{Hz}$ and $1800\,\mathrm{Hz}$ approximately. At these low angles of attack, the main noise mechanism is associated with the interaction between turbulent boundary layer fluctuations and the airfoil trailing edge. At $\alpha_g = 18°$, the boundary layer is partially separated, and the noise spectrum increases significantly between $200\,\mathrm{Hz}$ and $1000\,\mathrm{Hz}$; this corresponds to separation noise. Then at $\alpha_g = 25°$, where the boundary
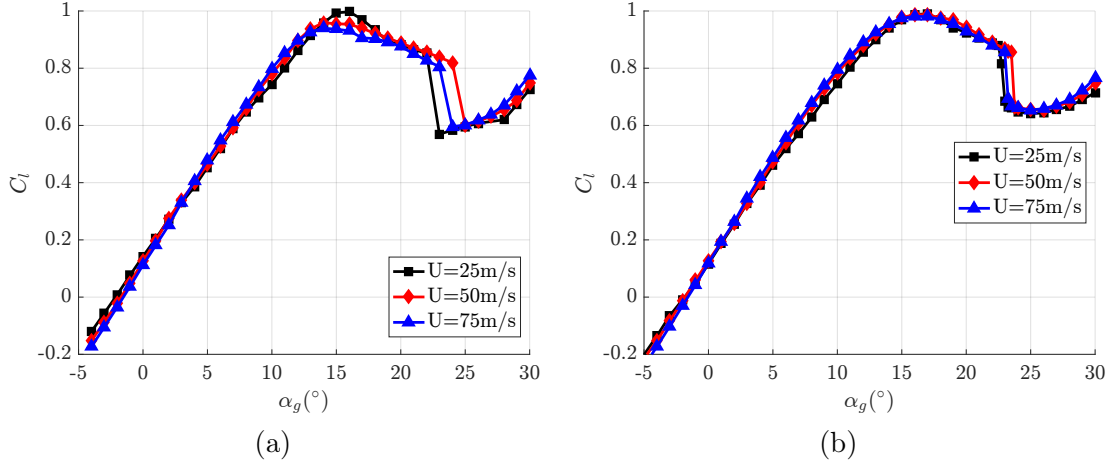
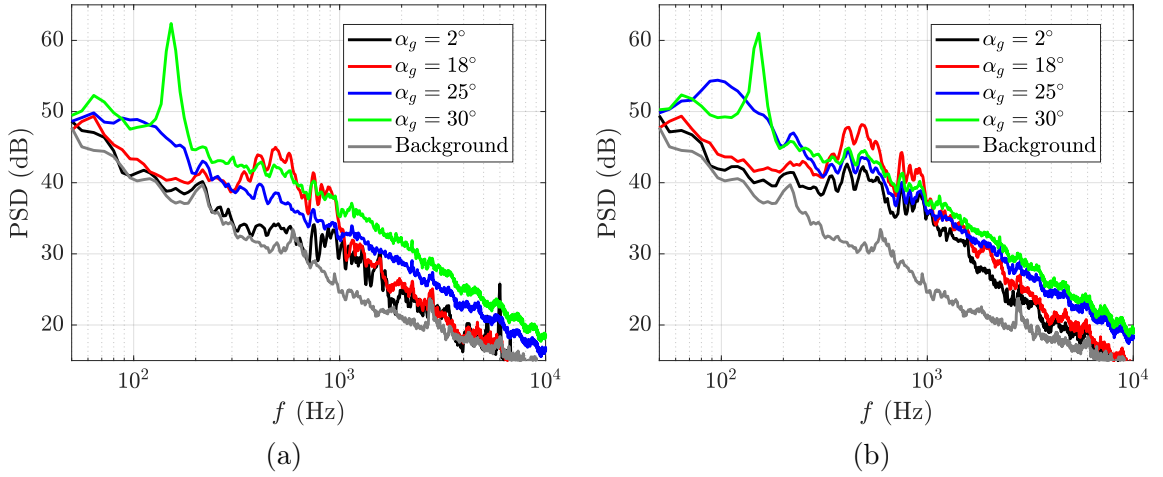Figure 4.1: Lift coefficients in the cases (a) with tripping and (b) with grid.

Figure 4.2: Power spectral densities of acoustic pressure in the cases (a) with tripping and (b) with grid.

layer is completely separated, the noise radiation is significantly above the background noise for all frequencies between 70 Hz and 10 kHz. This is sometimes called the light stall regime in the literature. Finally, at the maximum incidence angle of 30°, a strong narrowband peak appears around 160 Hz, which corresponds to a projected Strouhal number $Uc\sin\alpha_g/U \approx 0.19$. At this angle of attack, the airfoil behaves like a bluff body, which corresponds to the deep stall noise regime. In the case with grid, there is a significant increase in noise radiation between 200 Hz and 3 kHz. This can be attributed to turbulence interaction noise.

In order to evaluate the sensitivity of the acoustic spectrum to the inflow velocity, the PSD are plotted for three incoming velocities and the same four angles of attack
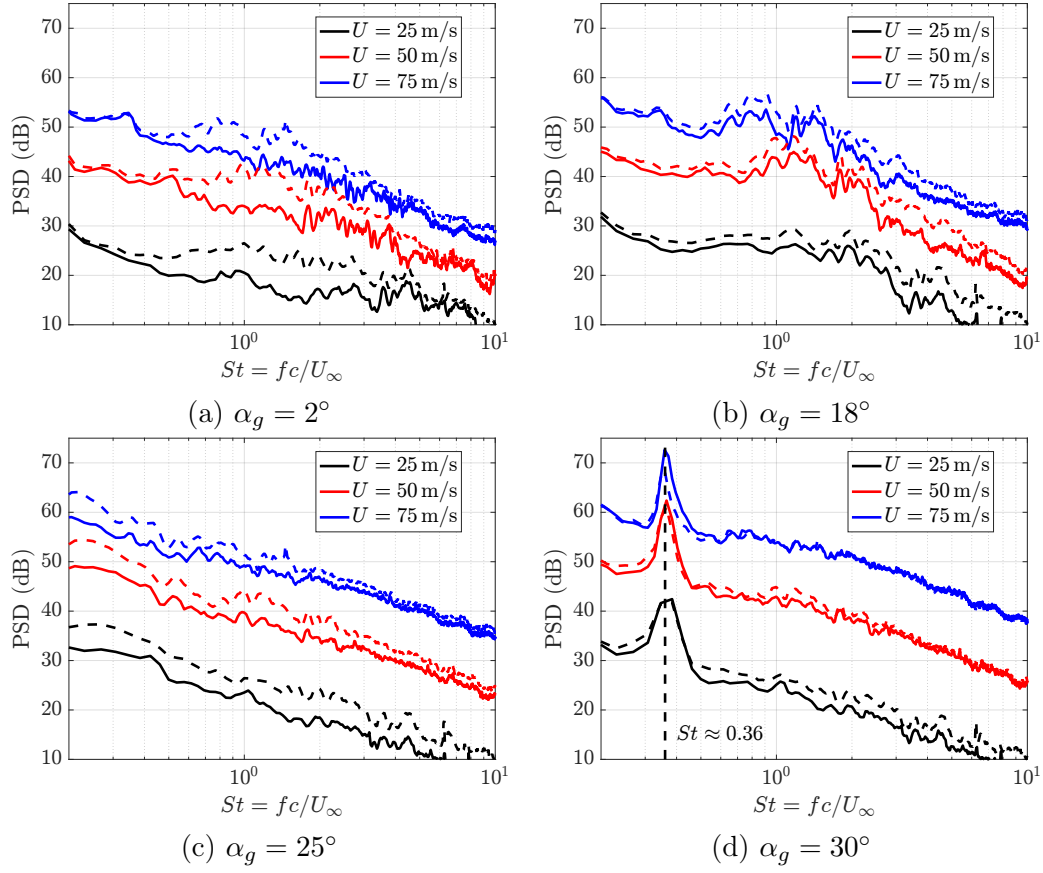
Figure 4.3: Power spectral densities of acoustic pressure. The solid lines correspond to the case with tripping, and the dashed lines correspond to the case with grid.
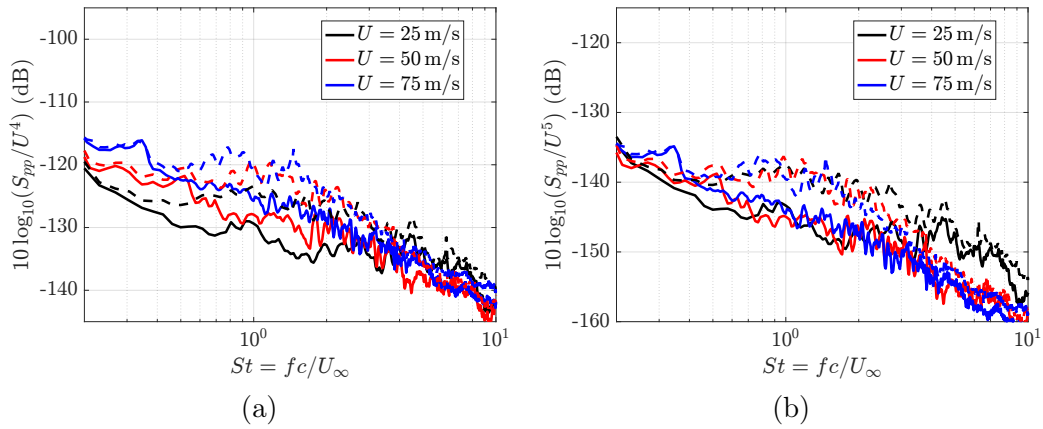

Figure 4.4: Power spectral densities of acoustic pressure at $\alpha_g = 2°$ normalized by (a) U^4 and (b) U^5. The solid lines correspond to the case with tripping, and the dashed lines correspond to the case with grid.
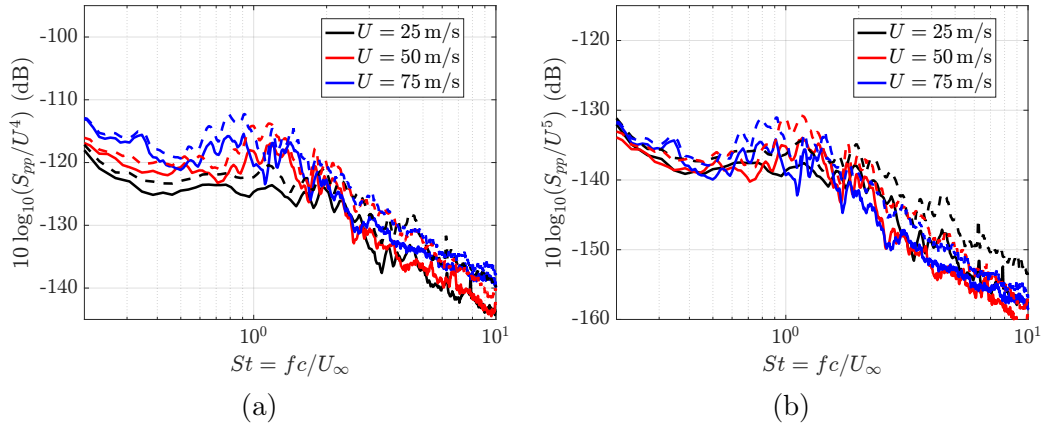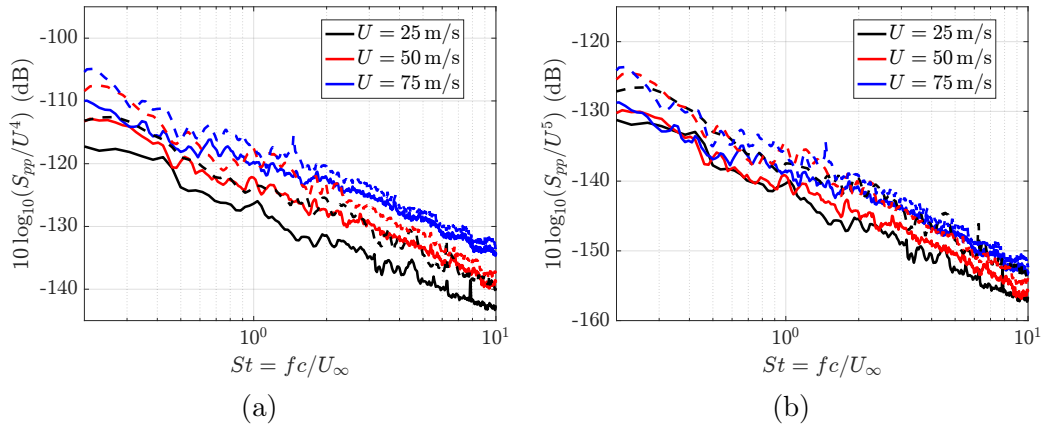
Figure 4.5: Same as Figure 4.4 at $\alpha_g = 18°$.
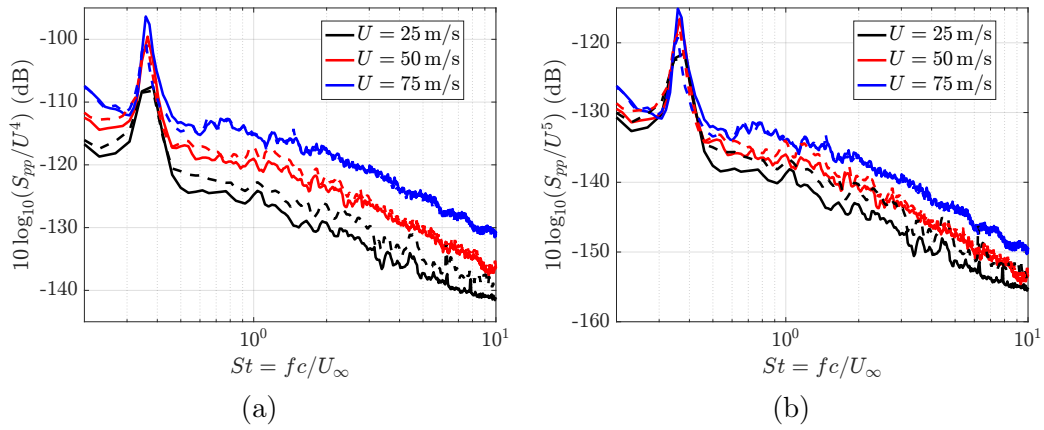

Figure 4.6: Same as Figure 4.5 at $\alpha_g = 25°$.

Figure 4.7: Same as Figure 4.5 at $\alpha_g = 30°$.

39

in Figure 4.3. Note that the background noise is not plotted in this figure. As seen in Figure 4.2 for $U = 50\,\text{m/s}$, the signal to noise ratio is quite low at $\alpha_g = 2°$ for the other flow velocities, and increases for larger incidence angles. The difference between the cases with and without turbulence grid is maximal for $\alpha_g = 2°$, with an increase of up to $8\,\text{dB}$ that is associated to turbulence interaction noise. At an incidence angle of $30°$, a tonal peak is consistently found for a Strouhal number of 0.36, corresponding to a projected Strouhal number $Uc\sin\alpha_g/U \approx 0.19$. The influence of the turbulence grid is small in this deep stall noise regime.

As pointed out by Roger and Moreau [20], a scaling law can be sought by normalizing the PSD of the acoustic pressure by U^n, with n an exponent to determine. For trailing edge noise, it is admitted that $n = 5$ provides the best scaling at low frequencies (compact airfoil), while $n = 4$ yields better results at high frequencies. This corresponds to integrated energy levels scaling with the powers 6 and 5 of the incoming velocity, respectively. In Figures 4.4 to 4.7, the two scaling laws are tested for the same four angles of attack as in Figure 4.3. At $\alpha_g = 2°$, all curves overlap at high frequencies using the U^4 scaling, which is expected as trailing edge noise dominates in this frequency range. At low frequencies, we observe that two families of curves emerge using the U^5 scaling. In the case with grid, turbulence ingestion noise is dominant while trailing edge noise is dominant in the case with tripping. At $\alpha_g = 18°$ and $25°$, the scaling is less convincing, using either exponent. At $\alpha_g = 30°$, on the other hand, a relatively good overlap is obtained around the low-frequency peak using the U^5 scaling.
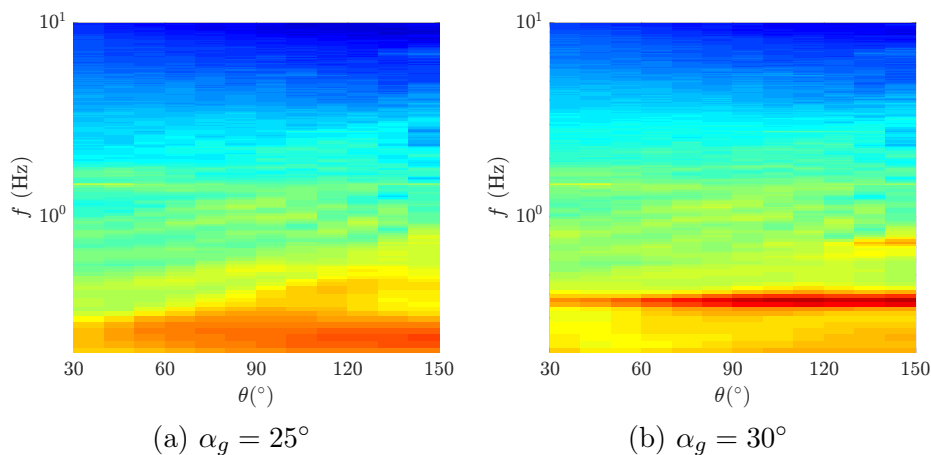

(a) $\alpha_g = 25°$ (b) $\alpha_g = 30°$

Figure 4.8: Power spectral densities of acoustic pressure for all 13 radiation angles in the case with grid. The color bar is between 20 and $65\,\text{dB}$

The PSD for all the microphones of the array are plotted in Figure 4.8 in the case with grid. For both $\alpha_g = 25°$ and $\alpha_g = 30°$, there is a stronger noise radiation upstream, for angles around $120°$. In the deep stall noise regime, for $\alpha_g = 30°$, the tonal peak at $St \approx 0.36$ is present at all angles, and its amplitude increases when θ increases. A second peak at $St \approx 0.72$ appears for radiations angles above $120°$.

2   Effect of the oscillation frequency on the acoustic radiation of a pitching airfoil

We focus here on the results for $U = 25\,\mathrm{m/s}$ and $50\,\mathrm{m/s}$ in the case with tripping, for the reduced frequencies given in Table 4.1. First, the evolution of the phase-averaged lift coefficient with the angle of attack is plotted in Figure 4.9 for all the reduced frequencies. The curve in the static regime is also shown as a reference. The curves for the oscillating airfoil follow the static airfoil curve up to the static stall angle around $15°$. Then, a lift overshoot is observed, that increases with the reduced frequency k, as classically observed in the literature; see Ref. [8] and references therein. When the angle of attack decreases from $30°$ the lift coefficient drops to values close to the static ones. The higher the reduced frequency, the later the boundary layer reattaches. Overall, the hysteresis loop strongly increases when k increases from 0.01 to 0.05 for $U = 25\,\mathrm{m/s}$, and from 0.005 to 0.025 for $U = 50\,\mathrm{m/s}$. Even though the reduced frequencies of 0.005 and 0.01 correspond to the quasi-static regime according to the literature, a significant increase of the hysteresis loop is seen between these two oscillation frequencies.

Table 4.1: Parameters associated with the six oscillating airfoil configurations.

U (m/s)	α_0 (°)	α_1 (°)	f_o (Hz)	k	$k^\star$
25	15	15	0.66	0.01	2.6×10^{-3}
25	15	15	1.66	0.025	6.5×10^{-3}
25	15	15	3.32	0.05	1.3×10^{-2}
50	15	15	0.66	0.005	1.3×10^{-3}
50	15	15	1.33	0.01	2.6×10^{-3}
50	15	15	3.32	0.025	6.5×10^{-3}

To better assess the effect of the Reynolds number on the evolution of the lift coefficient, the curves are compared in Figure 4.10 for reduced frequencies of 0.01 and 0.025. The curves are quite similar, although the lift coefficient reaches slightly higher values at large increasing angles of attack for $U = 25\,\mathrm{m/s}$. Also, the boundary layer tends to reattach at lower decreasing angles of attack for $U = 25\,\mathrm{m/s}$.

Phased-averaged spectrograms of acoustic pressure are calculated with a frequency resolution of 6 Hz and an overlap of 80%. The temporal resolution correspond to $t_c/50$, where $t_c = 1/f_0$ is the oscillation period. The spectrograms are plotted in Figure 4.11 for all cases except the reduced frequency $k = 0.05$ for $U = 25\,\mathrm{m/s}$, because this measurement is contaminated by motor noise. For the quasi-static regimes at $k = 0.005$ and $k = 0.01$, a strong broadband noise increase is visible at $f_0 t = 0.4$, corresponding to the complete boundary layer separation (light stall noise). Then, a narrowband peak around a Strouhal number of 0.36 is present up to $f_0 t = 0.7$ (deep stall noise), followed by a broadband noise associated with the boundary layer reattachment. For the reduced frequency $k = 0.025$, which is an intermediate case between the quasi-static and the dynamic regimes, a similar
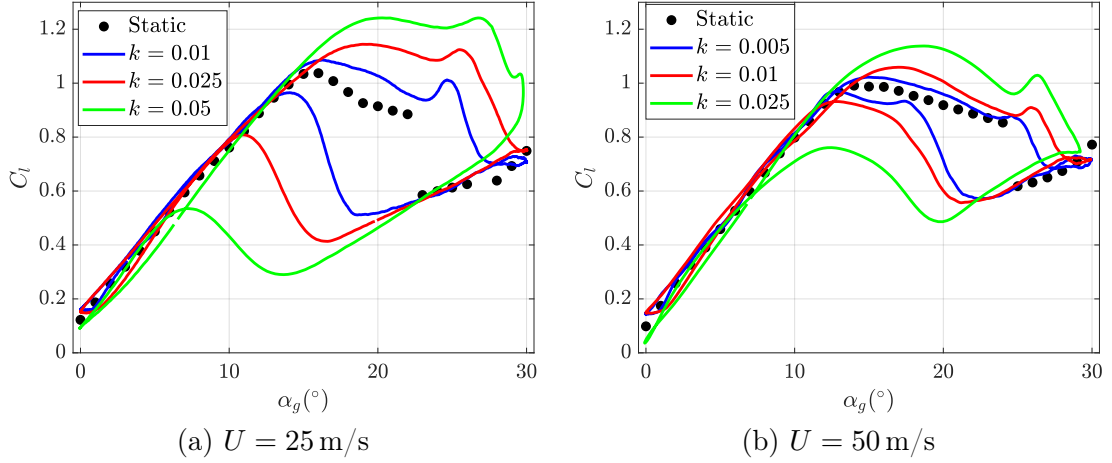
(a) $U = 25\,\text{m/s}$ (b) $U = 50\,\text{m/s}$

Figure 4.9: Phased-averaged lift coefficient for the oscillating airfoil at different reduced frequencies k.

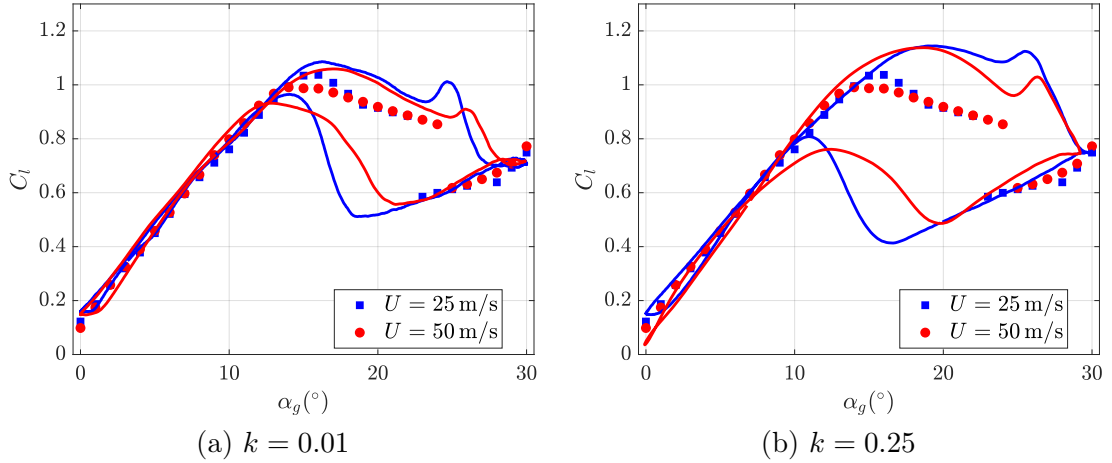(a) $k = 0.01$ (b) $k = 0.25$

Figure 4.10: Comparison of the phased-averaged lift coefficient for $U = 25\,\text{m/s}$ and $U = 50\,\text{m/s}$ for the oscillating airfoil (solid lines). The symbols correspond to the data for the static airfoil.

shape is observed but with stronger levels, especially during the boundary layer separation around $f_0 t = 0.4$.

The Overall Sound Pressure Level (OASPL) is defined as:

$$\text{OASPL} = 10 \log_{10} \left(\frac{1}{p_{ref}^2} \int_{f_1}^{f_2} S_{pp} df \right), \tag{4.1}$$

with $p_{\text{ref}} = 20\,\mu\text{Pa}$ the acoustic reference pressure and $f_1 = 70$ Hz and $f_2 = 1000$ Hz. These values are chosen in order to capture the noise amplitude variations in the stall
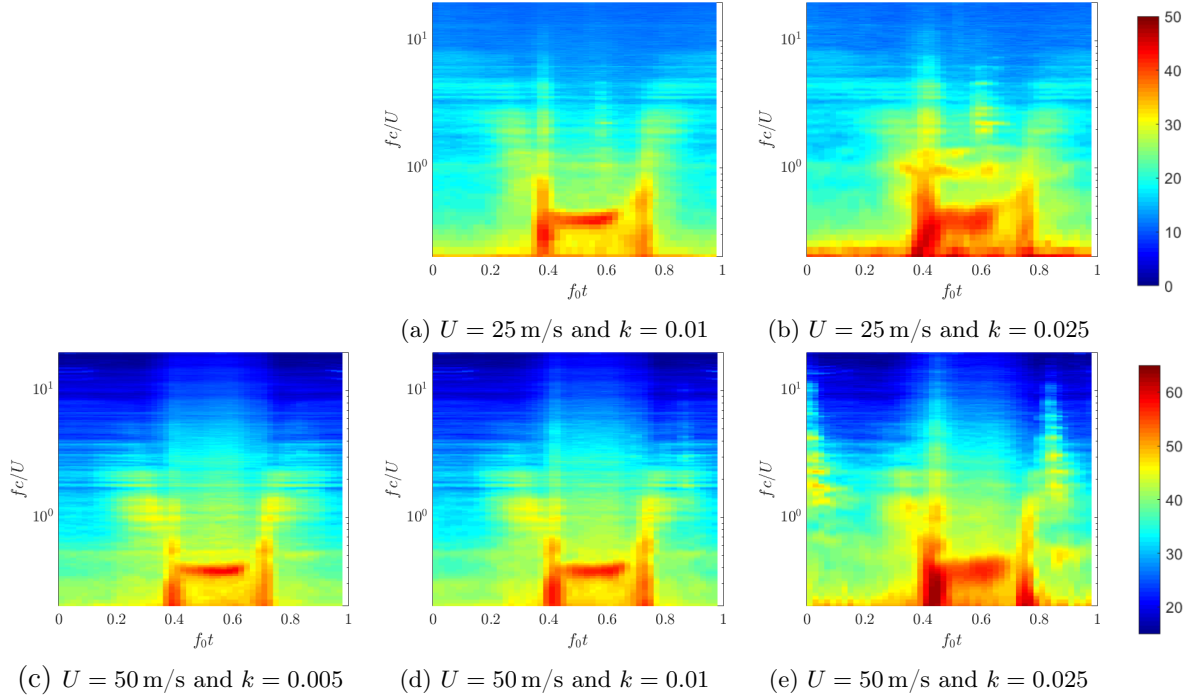
(a) $U = 25\,\mathrm{m/s}$ and $k = 0.01$ (b) $U = 25\,\mathrm{m/s}$ and $k = 0.025$

(c) $U = 50\,\mathrm{m/s}$ and $k = 0.005$ (d) $U = 50\,\mathrm{m/s}$ and $k = 0.01$ (e) $U = 50\,\mathrm{m/s}$ and $k = 0.025$

Figure 4.11: Phased-averaged spectrograms of acoustic pressure for different reduced frequencies k and different reduced frequencies U.

noise frequency range. The phase-averaged OASPL during the pitching motion is shown in Fig. 4.12a at $U = 50\,\mathrm{m/s}$ and various reduced frequencies, with $f_0 t = 0$ and $f_0 t = 0.5$ corresponding to $\alpha_{d,g} = 0°$ and $\alpha_{d,g} = 30°$, respectivelly. For every reduced frequency, the OASPL is progressivelly increasing before the onset of stall. Maximums of OASPL are then observed at the stall onset and near flow reattachment, corresponding to the broadband noises obtained near the critical stall and reattachment angles. In between these instants, a decrease of the OASPL is observed, corresponding to the dynamic deep-stall noise regime. For $k = 0.005$ and $k = 0.01$, similar OASPL curves are obtained. However for $k = 0.025$, an increase of the width and maximum value of the stall onset OASPL peak is observed. The peak reaches OASPL = 78 dB for $k = 0.005$ and OASPL = 83 dB for $k = 0.025$. Moreover, increasing the reduced frequency leads to a delay of the maximum of the peak, the maximum taking place at $f_0 t = 0.38$ for $k = 0.005$ and $f_0 t = 0.43$ for $k = 0.025$.

Effects of the airfoil shape on the OASPL are also investigated in Fig. 4.12b for $k = 0.01$. For the NACA63$_3$418, the stall onset OASPL peak appears to have lower amplitude and be delayed to greater angles of attack compared to the NACA0012. On the same way, the OASPL hump centered at $f_0 t \sim 0.58$ corresponding to the deep-stall regime also has a lower amplitude for the cambered airfoil. In the same way, the OASPL peak at flow reattachment takes place earlier for the NACA63$_3$418 than for the NACA0012, but the peaks have the same amplitude. The duration of the stalled phase
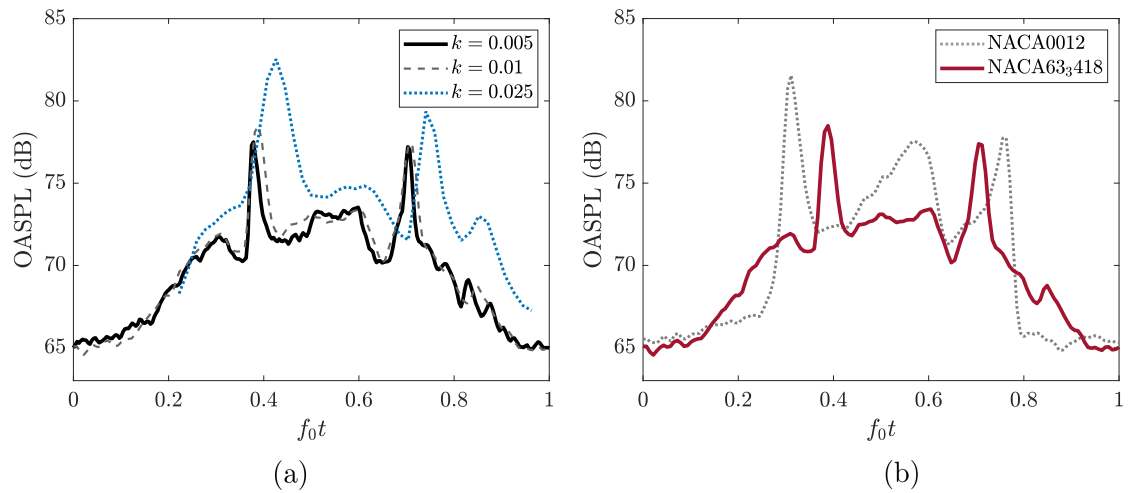
Figure 4.12: Phase-averaged OASPL during the dynamic stall phenomenon for (a) the NACA63$_3$418 and various reduced frequencies, and (b) the two airfoils and $k = 0.01$. For the cambered airfoil and $k = 0.025$, the OASPL is cut for angles where the motor noise is dominating.

of the cycle is thus shorter for the cambered airfoil. For the NACA0012, the OASPL is flat before stall and after flow reattachement ($f_0t < 0.2$ and $f_0t > 0.8$) and stall leads to an abrupt increase of OASPL, from OASPL = 67 dB at $f_0t = 0.24$ to OASPL = 82 dB at $f_0t = 0.31$. For the NACA63$_3$418, a progressive increase of OASPL is observed before stall onset due to the gradual flow separation on the suction side of the airfoil, leading this airfoil to be the noisiest before the stall onset and after flow reattachment.

Results of the third campaign with TR-PIV using a NACA 63$_3$418 airfoil

In this chapter, results from the third campaign using a NACA 63$_3$418 airfoil are presented. More details can be found in the PhD thesis of Lisa Sicard [23].

1 Identification of airfoil stall noise sources in static conditions

1.1 Characterization of airfoil noise spectra and flow topology

Let us first compare the acoustic signatures measured at different effective angles of attack α_e. The power spectral densities (PSD) of the acoustic pressure S_{pp} averaged over the ten acquisition runs are plotted in Figure 5.1 for five angles of attack and for the background noise. As the background noise is dominant for frequencies below 70 Hz, the acoustic analysis is restriced to frequencies between 70 Hz and 1500 Hz. First, at zero incidence, the signal to noise ratio is low, with a broadband noise radiation emerging above 600 Hz. This corresponds to trailing edge noise associated with an attached turbulent boundary layer. At the higher angles of attack $\alpha_e = 10.2°$ and at $\alpha_e = 13.4°$, the noise radiation increases significantly between 400 Hz and 1000 Hz. This is characteristic of the light stall noise [2]. At the highest angle of attack of $\alpha_e = 26.3°$, a narrow-band peak of high amplitude around 162 Hz appears, which is a typical feature of the deep stall noise [2]. The noise radiation at $\alpha_e = 23.8°$ shows an intermediate behavior, with a decrease in the amplitude of the light stall noise and the appearance of a broadband hump around 240 Hz. Raus *et al.* [22] have shown that the boundary layer separation point gradually moves from the trailing edge to the leading edge between $\alpha_e = 10.2°$ and $\alpha_e = 23.8°$, which is consistent with these noise radiation behaviors.

Let us now focus on the deep stall noise regime at $\alpha_e = 26.3°$. In order to visualize the mean flow topology, the ensemble-averaged streamlines are plotted in Figure 5.2, along with two components of the Reynolds tensor. The flow is completely separated from the leading edge on the airfoil suction side. The wake presents two recirculation zones. The first one is bounded by the leading edge shear layer and is associated to a separation
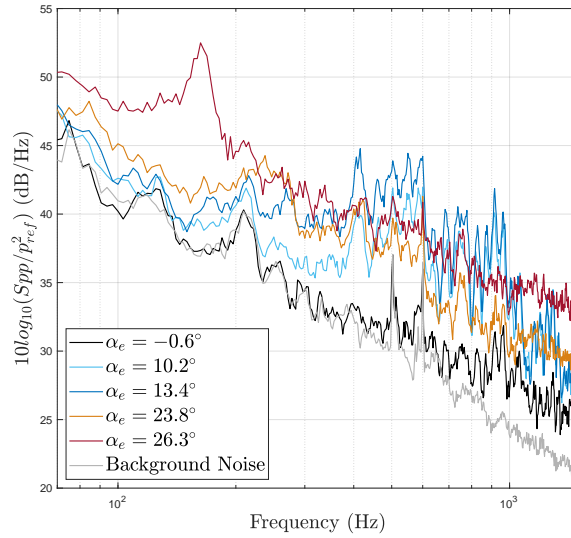
45

Figure 5.1: PSD of far-field sound pressure for different angles of attack averaged over the ten independent runs.
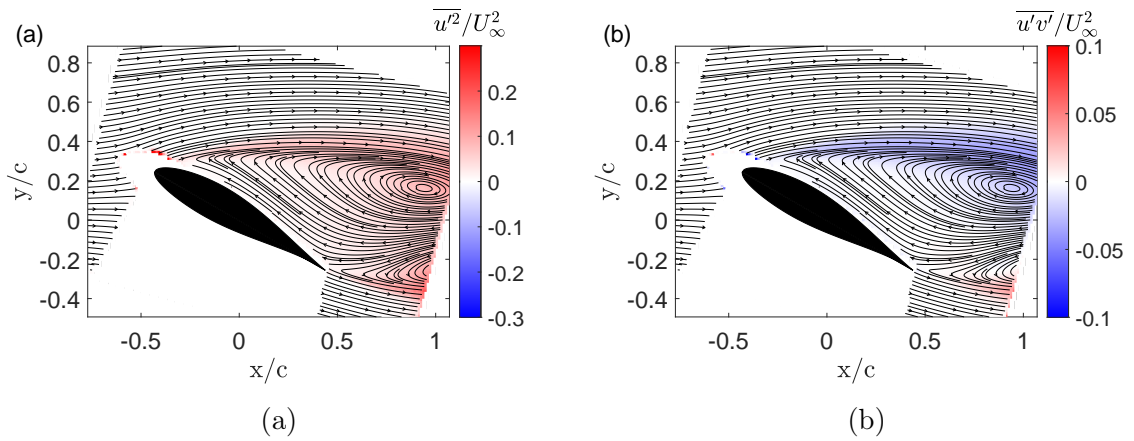

Figure 5.2: Streamlines of the mean flow with (a) the $\overline{u'^2}$ component of the Reynolds tensor and (b) the $\overline{u'v'}$ component of the Reynolds tensor averaged over the ten independent runs at $\alpha = 26.3°$.

bubble reattaching to the trailing edge. The second one is located near the trailing edge and results from the interaction of the separation bubble with the flow coming from the pressure side of the airfoil. Both recirculation zones have opposite circulation. If the latter is small, the former is too long to fit in the PIV field of view. Nevertheless, its length can be estimated to be of the same order of magnitude as the airfoil chord. The Reynolds stress distributions highlight the presence of high turbulent activity in the shear layers starting at the leading and trailing edges.

As turbulent coherent structures play an important role in the noise produced by a flow, we seek to identify the turbulent structures present in the wake at $\alpha_e = 26.3°$. This identification is performed using the Eulerian vortex detection criterion Γ_2. This criterion introduced by Graftieaux *et al.* [24] involves a scalar function that varies within the range of -1 to 1, with its extrema highlighting the spatial position of vortices centers. Positive values indicate the presence of a vortex rotating clockwise, while negative values indicate the presence of a vortex rotating counterclockwise.

Figures 5.3(a) and (b) show the spatial distributions of the percentages of time associated with positive and negative vortices respectively. A threshold of ± 0.85 is used and the integration area includes 3×3 PIV points, following Mulleners and Raffel [25]. We observe in Figures 5.3(a) clockwise-rotating vortices that are recurrently identified over time, that suggests the presence of a Kelvin-Helmholtz instability. On the other hand, Figures 5.3(a) shows the presence of counterclockwise-rotating vortex centers in the trailing edge shear layer, corresponding to a large-scale trailing edge vortex.
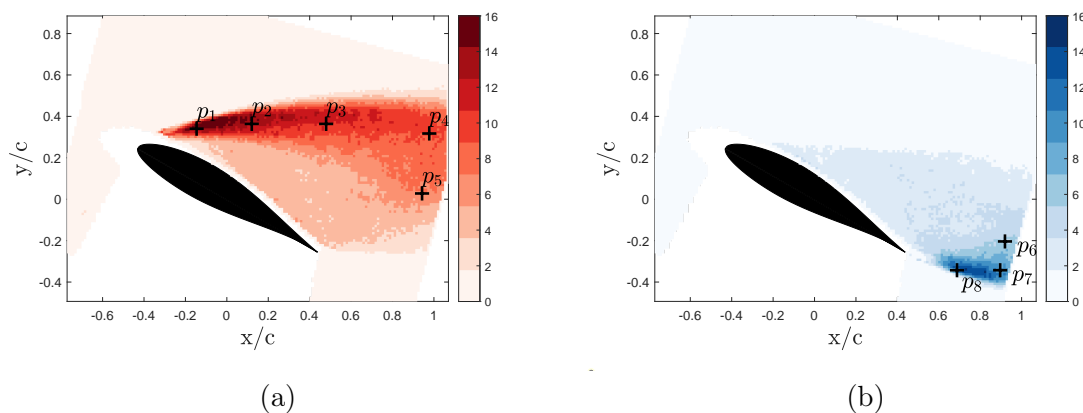

(a)   (b)

Figure 5.3: Spatial distribution of the percentage of time spent by Γ_2 in (a) positive values greater than a threshold of 0.85 and (b) negative values lower than a threshold of -0.85 during a data acquisition for an integration area comprising 3×3 PIV points for $\alpha_e = 26.3°$
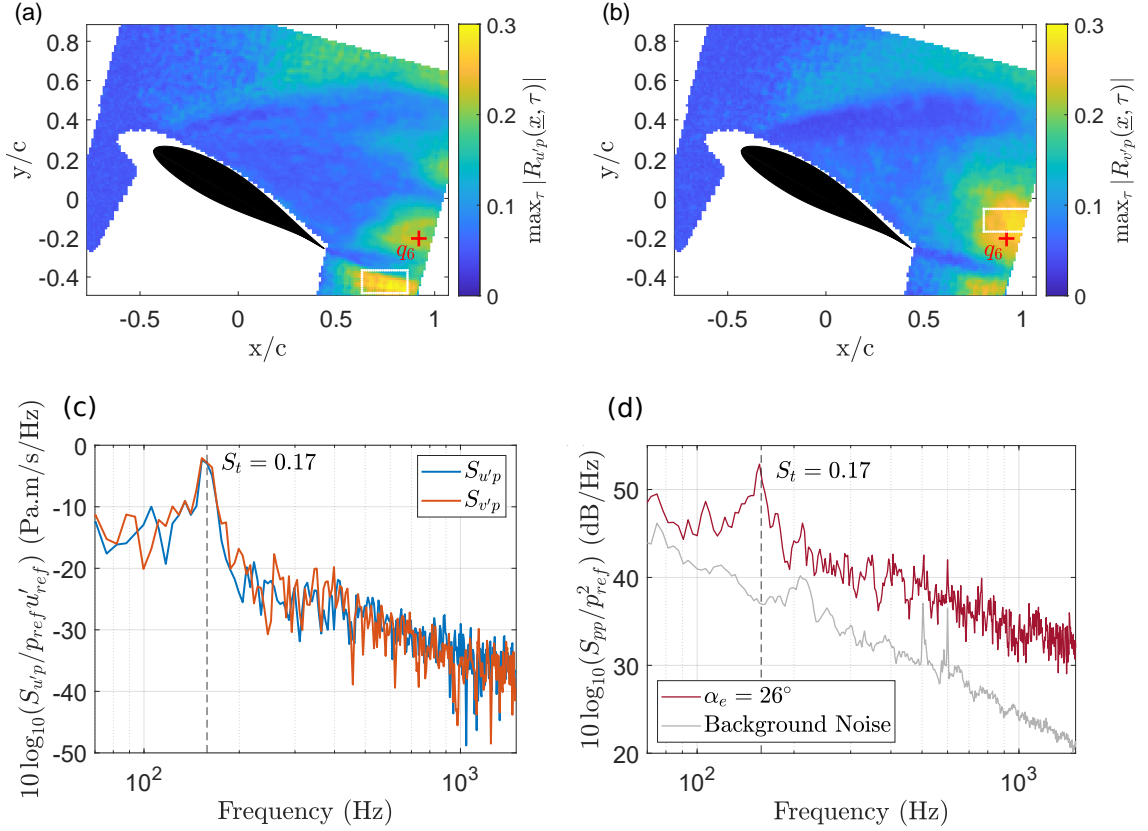
Figure 5.4: Top: Map of local maxima over τ of normalised correlations for longitudinal velocity fluctuations (a) and transverse velocity fluctuations (b) for one acquisition run. Bottom: (c) Local average of the CPSDs computed in the maximum correlation zone and (d) PSD of far-field acoustic pressure.

1.2 Identification of acoustic sources in deep stall conditions

In order to localize the acoustic sources in the flow, we now calculate the normalized cross-correlations between the velocity fluctuations u' or v' and the acoustic pressure p:

$$R_{\mathrm{u'p}}(\underline{x}, \tau) = \frac{1}{N_t} \frac{\sum_{i=1}^{N_t} u'(\underline{x}, t_i) \, p\,(t_i - \tau)}{\sigma(u')\sigma(p)}, \tag{5.1}$$

$$R_{\mathrm{v'p}}(\underline{x}, \tau) = \frac{1}{N_t} \frac{\sum_{i=1}^{N_t} v'(\underline{x}, t_i) \, p\,(t_i - \tau)}{\sigma(v')\sigma(p)}, \tag{5.2}$$

with $\sigma(X)$ the standard deviation of X. Figures 5.4(a) and (b) show the maximum cross-correlation coefficients obtained at each point in space for the longitudinal and transverse fluctuations over all the correlation delay τ for one run at $\alpha_{\mathrm{e}} = 26.3°$ respectively. The maxima of the cross correlations for the two velocity components are located in two

48

different zones downstream of the trailing edge, highlighted by white rectangles.

In order to obtain more information about these correlations, we calculate the cross power spectral density (CPSD) $\overline{S_{u'p}}$ and $\overline{S_{v'p}}$ between the velocity fluctuations u' and v', respectively, and the acoustic pressure for the points located in the white rectangles that contain 10×20 points centered around the spatial maximum of the correlation maps. The local average of the CPSDs $\overline{S_{u'p}}$ and $\overline{S_{v'p}}$ are plotted in Figure 5.4(c), and the PSD of the acoustic pressure is plotted in Figure 5.4(d). Note that the spectrum plotted in Figure 5.4(d) is slightly different from the one plotted in Figure 5.1 as it is calculated over a single run. It appears that both $\overline{S_{u'p}}$ and $\overline{S_{v'p}}$ contain the same amplitude peak at a frequency of 158 Hz, that is also present in the acoustic spectrum of Figure 5.4(d). This peak frequency corresponds to a projected Strouhal number $St = fc \sin \alpha_e / U$ of 0.17, close to the typical values corresponding to the bluff body Bénard-von Kármán vortex shedding. Thus, at high angles of attack, the NACA 63_3418 airfoil behaves like a bluff body, and deep stall noise is strongly linked to a structure oscillating around a Strouhal number of 0.17, located downstream of the trailing edge in the airfoil wake.

2 Results in dynamic conditions

2.1 Time-frequency analysis of the acoustic signals

In this section, we consider the noise radiated by the oscillating airfoil. The analysis is first performed over 100 oscillation periods for various reduced frequencies k. This allows us to calculate phase-averaged spectrograms over a large number of cycles, as shown in Figure 5.5. Spectrograms are computed using a short-term Fourier transform with 80% overlap with various window sizes that yield time resolutions of 14 ms, 6 ms and 3 ms respectively. The results are similar to the ones obtained by Raus $et\ al.$ [22] using an instrumented NACA $63_3 - 418$ airfoil. The main difference is that the motor noise issues that contaminated the acoustic results at high oscillating frequencies in Raus $et\ al.$ [22] have now been solved.

For the reduced frequency $k = 0.01$, corresponding to the quasi-static regime, we retrieve the same acoustic regimes as in Figure 5.1 in static conditions. The noise levels are low for small angles of attack, and a broadband radiation between 400 Hz and 1000 Hz emerges when the angle of attack exceeds approximately 15°, corresponding to the light stall noise. This pattern is also retrieved during the descending phase. Close to the maximum angle of attack of 30°, a spectral peak close to 160 Hz is clearly present, corresponding to the deep stall noise. In-between these two regimes, a broadband noise radiation is present, that can probably be related to the complete boundary layer detachment and reattachment. Note that the spectrogram at the lowest reduced frequency of $k = 0.005$ (not shown here) is similar to the one at $k = 0.01$.

For the highest reduced frequency $k = 0.05$, corresponding to the dynamic regime, it is more difficult to distinguish the different phases. This can be due to a more complex flow topology, but also to the fact that a small number of samples are used in each block of the short-term Fourier transform in order to obtain a small enough time resolution,

which means that the frequency resolution is degraded. In any case, it is clear that the radiated noise levels are significantly stronger in this regime compared to the quasi-static regime. For the intermediate reduced frequency $k = 0.025$, the pattern is closer to the quasi-static regime, with noise levels that are in-between the two extreme cases.
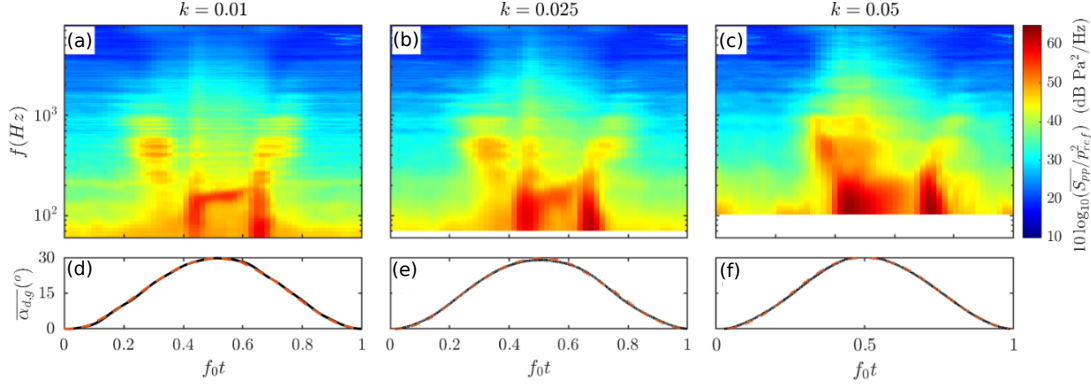

Figure 5.5: (a-b-c) Phase-averaged spectrograms of far-field acoustic pressure and (d-e-f) phase-averaged angle of attack for three reduced frequencies k. The overbar denotes phase-averaging.

2.2 Phase-averaged vorticity

In static conditions, we have identified that the turbulent structures in the wake of the airfoil, linked to the interaction between the shear layers emanating from the leading edge and the trailing edge, are associated to the radiated noise. In order to visualize the evolution of these shear layers during the airfoil oscillation in dynamic conditions, each oscillation is divided into 20 segments, and the vorticity field is phased-averaged using all available runs.

Figure 5.6 shows the phase-averaged normalized vorticity $\omega c / U_\infty$ for the 12 segments with the highest angle of attack for the lowest oscillation frequency ($k = 0.005$). We observe that the shear layer with positive vorticity remains close to the airfoil suction side up to $\overline{\alpha} = 17.3°$. Above this angle the flow separation becomes more important, until the separation point reaches the leading edge for $\overline{\alpha} = 29.7°$, close to the highest incidence angle. During the descending motion, the shear layer reattaches around $\overline{\alpha} = 17.5°$. Although this case is considered as quasi-static, an hysteresis can be clearly seen by comparing the vorticity fields around $25.5°$ or $28.3°$ in ascending and descending motion.

To visualize the effect of the oscillation frequency on the flow topology, Figures 5.7 and 5.8 compare respectively the normalized vorticity fields between three reduced frequencies for the 4 segments with the highest angles of attack during the ascending and descending motion. The increase of the reduced frequency is associated with a stall delay. Also, for the some segments such as the one in Figure 5.8(b), the shear layer seems to oscillate between two states.
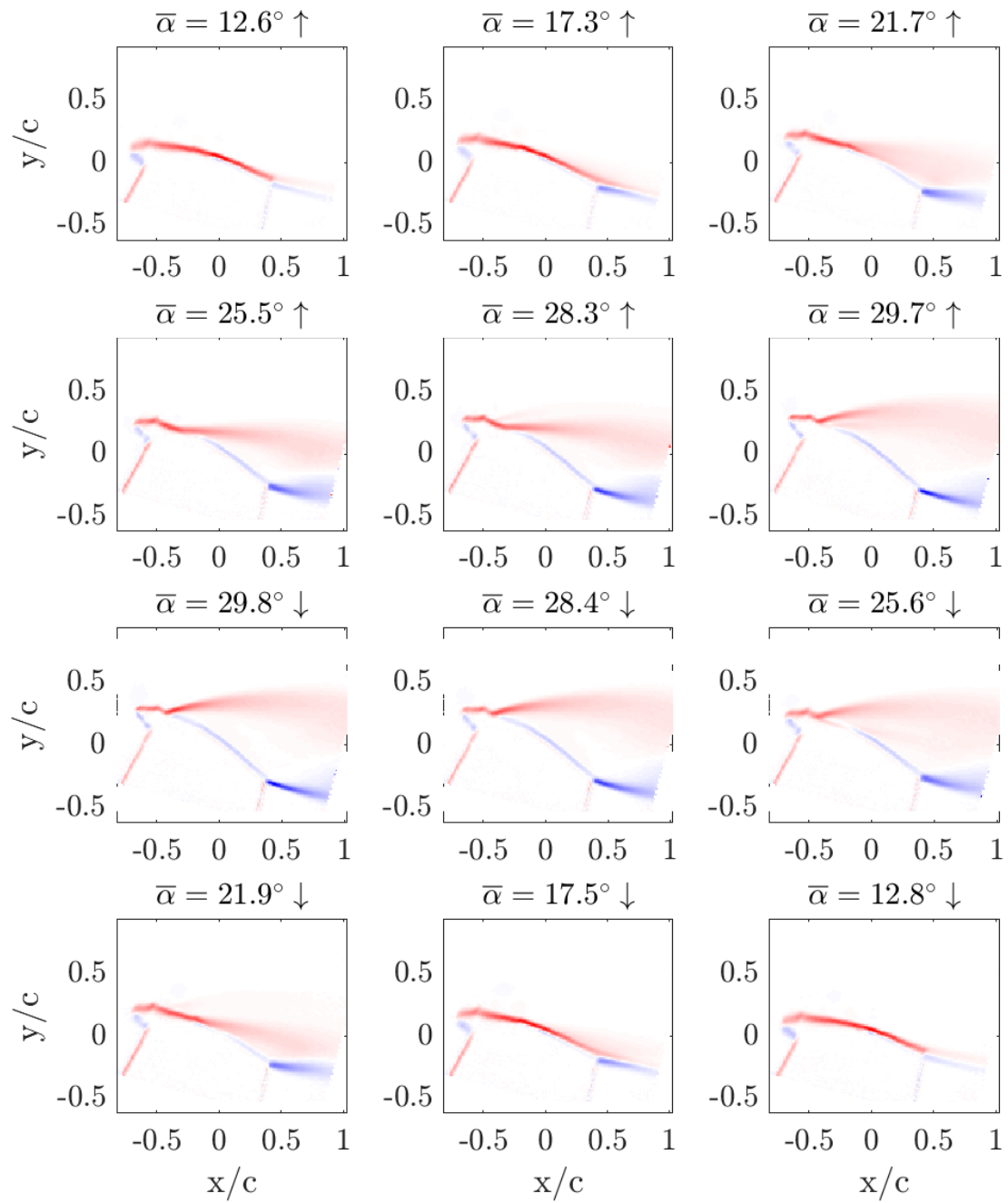
Figure 5.6: Phase-averaged normalized vorticity $\omega c/U_\infty$ for various segments at $k = 0.005$. The colorbar is between -0.05 and 0.05.
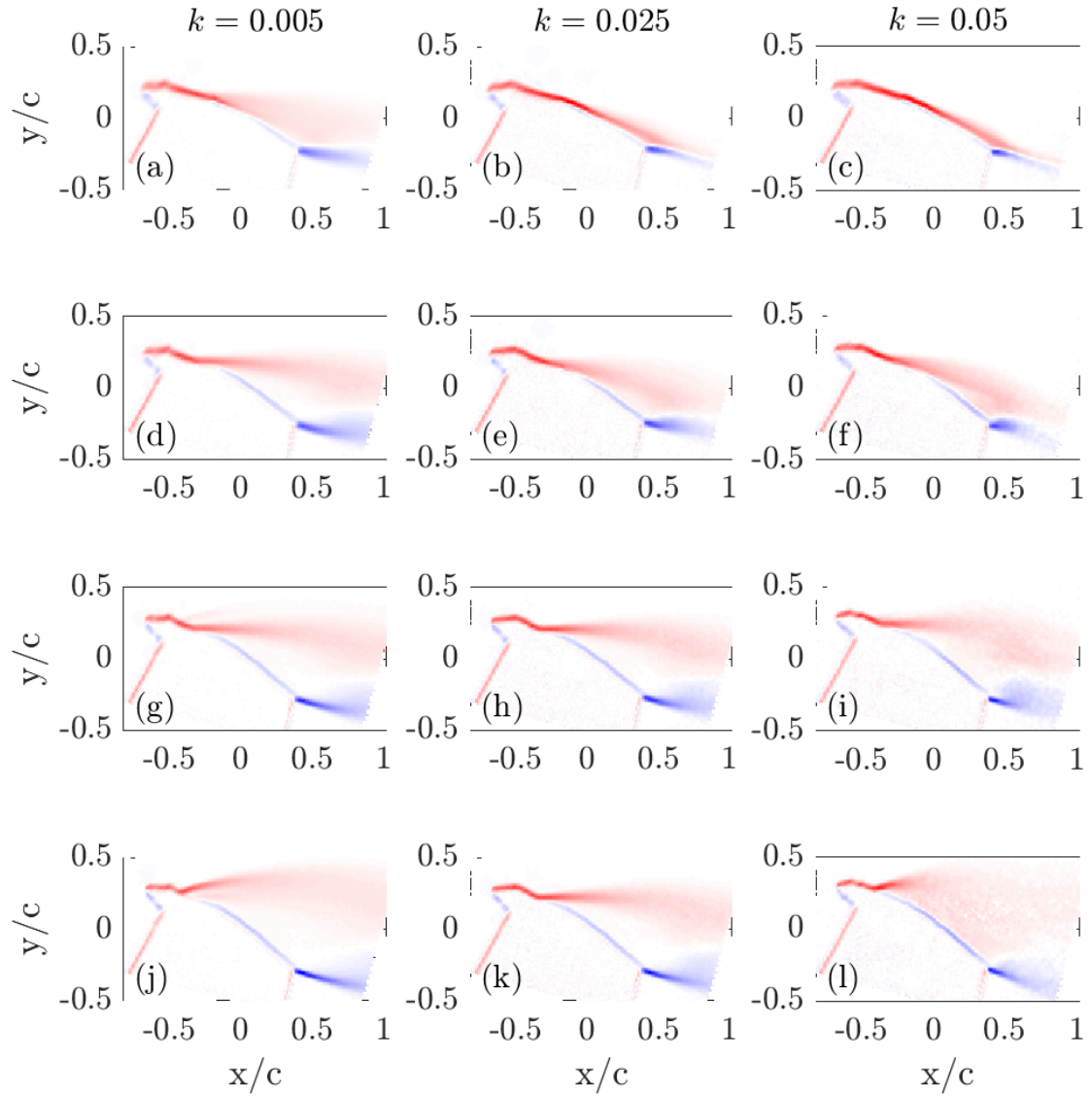
Figure 5.7: Phase-averaged normalized vorticity $\omega c/U_\infty$ for the reduced frequencies $k = 0.005$, $k = 0.025$ and $k = 0.05$ for 4 different segments during the ascending motion of the airfoil: (a-c) $\overline{\alpha} \approx 21.7°$, (d-f) $\overline{\alpha} \approx 25.5°$, (g-i) $\overline{\alpha} \approx 28.3°$, (j-l) $\overline{\alpha} \approx 29.7°$. The colorbar is between -0.05 and 0.05.
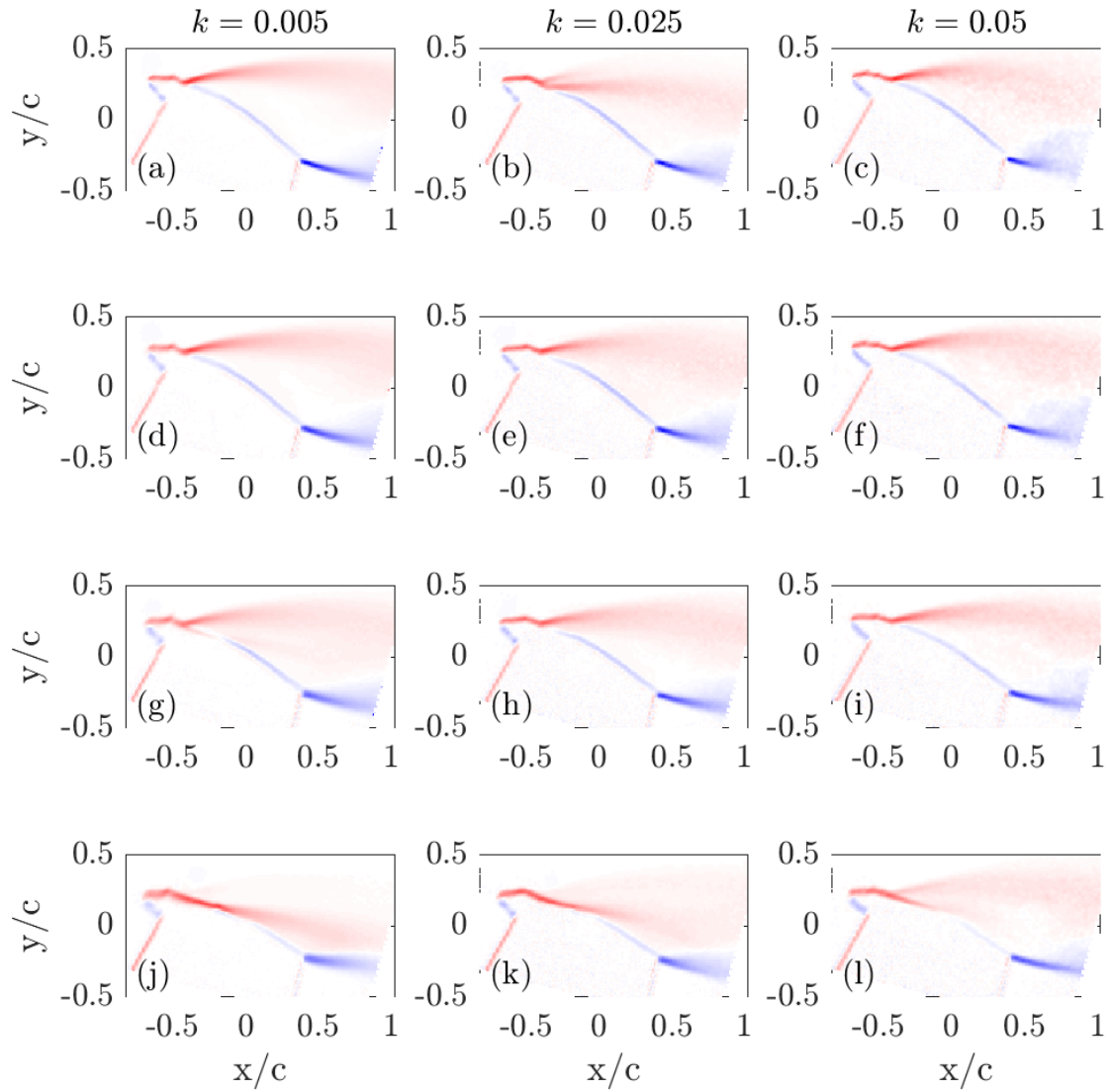
Figure 5.8: Phase-averaged normalized vorticity $\omega c/U_\infty$ for the reduced frequencies $k = 0.005$, $k = 0.025$ and $k = 0.05$ for 4 different segments during the descending motion of the airfoil: (a-c) $\overline{\alpha} \approx 29.8°$, (d-f) $\overline{\alpha} \approx 28.4°$, (g-i) $\overline{\alpha} \approx 25.6°$, (j-l) $\overline{\alpha} \approx 21.9°$. The colorbar is between -0.05 and 0.05.

Conclusion and perspectives

Within the framework of the PIBE project (Predicting the Impact of Wind Turbine Noise), an important experimental database has been collected in order to characterize airfoil stall noise both in static and dynamic regimes. Experiments have been performed with two different instrumented airfoil profiles, with different turbulence intensities and at different chord-based Reynolds numbers. In addition, synchronized flow and acoustic measurements have been obtained to identify the coherent aerodynamic structures responsible for the noise radiation. This database will be made available to the scientific community to enable stall noise to be better understood, modeled and mitigated in the future.

Several perspectives can be drawn for the coming years. Firstly, we keep on working on the identification of stall noise sources in the dynamic regime using correlation techniques as well as Proper Orthogal Decomposition (POD) tools. Secondly, amplitude modulations recorded during the *in situ* experimental campaign, and described in the final report of WP2, could be analyzed to identify the relationship between the occurrence of dynamic stalls and the weather and operational conditions of the turbine. Finally, a stall noise model could be proposed and implemented in the comprehensive wind turbine noise model developed during the PhD theses of Yuan Tian [26] and David Mascarenhas [27].

Bibliography

[1] Stefan Oerlemans. Effect of wind shear on amplitude modulation of wind turbine noise. *International Journal of Aeroacoustics*, 14(5-6):715–728, 2015.

[2] S. Moreau, M. Roger, and J. Christophe. Flow features and self-noise of airfoils near stall or in stall. In *15th AIAA/CEAS Aeroacoustics Conference (30th AIAA Aeroacoustics Conference)*, 2009.

[3] Franck Bertagnolio, Helge Aa. Madsen, Andreas Fischer, and Christian Bak. A semi-empirical airfoil stall noise model based on surface pressure measurements. *Journal of Sound and Vibration*, 387:127–162, January 2017.

[4] Giovanni Lacagnina, Paruchuri Chaitanya, Tim Berk, Jung-Hoon Kim, Phillip Joseph, Bharathram Ganapathisubramani, Seyed Mohammad Hasheminejad, Tze Pei Chong, Oksana Stalnov, Kwing-So Choi, Muhammad Farrukh Shahab, Mohammad Omidyeganeh, and Alfredo Pinelli. Mechanisms of airfoil noise near stall conditions. *Phys. Rev. Fluids*, 4:123902, 2019.

[5] L. Siegel, K. Ehrenfried, C. Wagner, K. Mulleners, and A. Henning. Cross-correlation analysis of synchronized piv and microphone measurements of an oscillating airfoil. *Journal of Visualization*, 21(3):381–395, 2018.

[6] Y. Mayer, B. Zang, and Mahdi Azarpeyvand. Aeroacoustic investigation of an oscillating airfoil in the pre- and post-stall regime. *Aerospace Science and Technology*, 103:105880, 2020.

[7] K. Mulleners and M. Raffel. Dynamic stall development. *Experiments in fluids*, 54:1469, 2013.

[8] David Raus, Benjamin Cotté, Romain Monchaux, Emmanuel Jondeau, Pascal Souchotte, and Michel Roger. Experimental study of the dynamic stall noise on an oscillating airfoil. *Journal of Sound and Vibration*, 537:117144, 2022.

[9] G. Yakhina. *Experimental study of the tonal trailing-edge noise generated by low-Reynolds number airfoils and comparison with numerical simulations*. PhD thesis, Ecole Centrale de Lyon, Lyon, 2017.

[10] Alex Laratro, Maziar Arjomandi, Benjamin Cazzolato, and Richard Kelso. Self-noise and directivity of simple airfoils during stall: An experimental comparison. *Applied Acoustics*, 127:133 – 146, 2017.

[11] Michel Roger. Microphone measurements in aeroacoustic installations. *Design and Operation of Aeroacoustic Wind Tunnel Tests for Ground and Air Transport STO-AVT-287. Von Karman Institute for Fluid Dynamics*, 2017.

[12] Ph. Devinant, T. Laverne, and J. Hureau. Experimental study of wind-turbine airfoil aerodynamics in high turbulence. *Journal of Wind Engineering and Industrial Aerodynamics*, 90(6):689 – 707, 2002.

[13] T. F. Brooks, D.S. Pope, and M.A. Marcolini. Airfoil self-noise and prediction. *NASA Reference Publication 1218*, 1989.

[14] R.W. Paterson, P.G. Vogt, M.R. Fink, and C. L. Munch. Vortex noise of isolated airfoils. *Journal of Aircraft*, 10(5):296–302, 1973.

[15] T. F. Brooks, M.A. Marcolini, and D.S. Pope. Airfoil trailing edge flow measurements and comparison with theory, incorporating open wind tunnel corrections. *9th Aeroacoustics Conference*, 1984.

[16] Henry Clifford Garner, EW Rogers, WE Acum, and EC Maskell. Subsonic wind tunnel wall corrections. Technical report, AGARDograph, 1966.

[17] Y. Mayer, B. Zang, and M. Azarpeyvand. Design of a kevlar-walled test section with dynamic turntable and aeroacoustic investigation of an oscillating airfoil. In *25th AIAA/CEAS Aeroacoustics Conference*, 2019.

[18] R E Sheldahl and P C Klimas. Aerodynamic characteristics of seven symmetrical airfoil sections through 180-degree angle of attack for use in aerodynamic analysis of vertical axis wind turbines. Technical report, Sandia National Lab., 1981.

[19] R.K. Amiet. Noise due to turbulent flow past a trailing edge. *Journal of Sound and Vibration*, 47(3):387 – 393, 1976.

[20] Michel Roger and Stéphane Moreau. Extensions and limitations of analytical airfoil broadband noise models. *International Journal of Aeroacoustics*, 9(3):273–305, 2010.

[21] Y. Mayer, Bin Zang, and Mahdi Azarpeyvand. Aeroacoustic characteristics of a NACA0012 airfoil for attached and stalled flow conditions. In *25th AIAA/CEAS Aeroacoustics Conference*, 2019.

[22] David Raus, Benjamin Cotté, Romain Monchaux, Lisa Sicard, Emmanuel Jondeau, Pascal Souchotte, and Michel Roger. Experimental characterization of the noise generated by an airfoil oscillating above stall. In *AIAA AVIATION 2021 FORUM*, page 2291, 2021.

[23] L. Sicard. *Identification expérimentale des sources acoustiques à l'origine du bruit de décrochage d'un profil de pale d'éolienne.* PhD thesis, Institut Polytechnique de Paris, 2023.

[24] Laurent Graftieaux, Marc Michard, and Nathalie Grosjean. Combining piv, pod and vortex identification algorithms for the study of unsteady turbulent swirling flows. *Measurement Science and technology*, 12(9):1422, 2001.

[25] Karen Mulleners and Markus Raffel. The onset of dynamic stall revisited. *Experiments in fluids*, 52:779–793, 2012.

[26] Y. Tian and B. Cotté. Wind turbine noise modeling based on amiet's theory: Effects of wind shear and atmospheric turbulence. *Acta Acustica united with Acustica*, 102:626–639, 2016.

[27] D. Mascarenhas, B. Cotté, and O. Doaré. Propagation effects in the synthesis of wind turbine aerodynamic noise. *Acta Acustica*, 7(23), 2023.